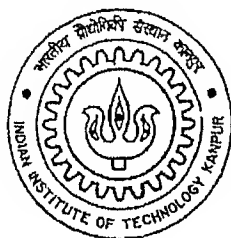


ONE-DIMENSIONAL PHYSICAL MODEL OF LASER SURFACE CLADDING

A Thesis Submitted
in Partial Fulfillment of the Requirements
for the Degree of
MASTER OF TECHNOLOGY

by

JOYE R



**DEPARTMENT OF MATERIALS AND
METALLURGICAL ENGINEERING
INDIAN INSTITUTE OF TECHNOLOGY KANPUR**

November, 1997

5 DEC 1997

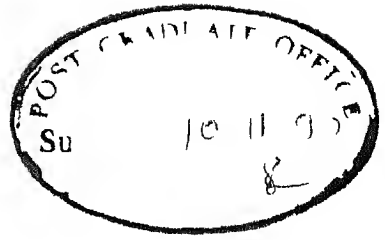
CENTRAL LIBRARY
I. I. T. KANPUR

Inv. No. **A** 124451



A124451

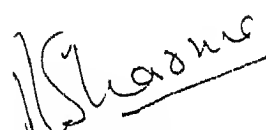
MME-1897-M-JCY-DIV 1



CERTIFICATE

It is certified that the work contained in the thesis entitled "*One Dimensional Physical Model of Laser Surface Cladding*", by *Joye R*, has been carried out under my supervision and that this work has not been submitted elsewhere for a degree

November 1997


Dr. R. C. Sharma
Professor,
Department of MME,
IIT, Kanpur

ACKNOWLEDGEMENT

I express my sincere gratitude to my thesis supervisor **Dr R C Sharma** for his guidance and support throughout this work. The time I spent with him is the most fruitful and potential learning period of my life. I am very grateful to his friendly and encouraging nature.

I express my sincere thanks to **Dr Rajiv Shekar** for his help in carrying out my thesis.

I express my sincere thanks to my friends **Mr S Senthil**, **Mr M G P Prasad**, **Mr Dixit** and **Mr Vinod Narang** for their help in my thesis.

My cordial thanks to my friends **Udhaya Shankar**, **Saravanan**, **Navaneet**, **Siva Gomathi**, **Sriram**, **Ravi(2)**, **Kali**, **Venkat**, **Anand(3)**, **Srim(2)**, **Rajesh(3)**, **Satya**, **Shailesh**, **Ashish**, **Rakesh**, **Kishore**, **Dhanabal**, **Balaji(2)**, **Pandi**, **Veera**, **Swami**, **Subash**, **Nagendran**, **Kalya**, **Palani**, **Govind**, **Fredric**, **Sundar**, **Supriya**, **Shaju**, **Vivek**, **Sameer**, **Krishnaraj**, **Rajarethnam**, **Muthu**, **Ramesh(2)**, **Sunil**, **Senthil(2)**, **Krishna Murthy**, **Jaya**, **Kingsly**, **Jayaraj**, **Bala**, and **BabuN** for making my stay at IIT Kanpur a pleasant and memorable one.

JOYE R

ABSTRACT

High power density, high beam diameter, and uniform laser beam processing is treated in one dimensional approximation by considering Stefan condition at the moving melt boundary. The exact turbulent behaviour of laser melted zone in laser cladding is not known. Hence modelling is done for the two extreme cases complete turbulence and no turbulence. The variation of melting rate with power density, thermal diffusivity and clad height are studied for both models and compared. A higher power density gives higher melting rate and is more economical. Maximum power density is limited by surface melt evaporation. The turbulent melting model is more realistic than the stagnant melting model and hence the actual melting time is expected to be closer to, but somewhat more than the melting time predicted by the turbulent melting model.

Contents

1	INTRODUCTION	1
2	LITERATURE REVIEW	4
2 1	Laser Material Interaction	4
2 2	Uniqueness of laser source	6
2 3	Laser Cladding	7
2 3 1	Methods of Laser Cladding	7
2 3 2	Clad substrate combination	8
2 3 3	Experimental Results	9
2 4	Mathematical Models	19
3	ONE DIMENSIONAL MODEL FOR LASER CLADDING	26
3 1	Introduction	26
3 2	Turbulent melting	27
3 3	Stagnant melting	34
4	RESULTS AND DISCUSSIONS	38
4 1	Introduction	38
4 2	Preheating	39

4 3	Turbulent Melting	41
4 4	Stagnant Melting	46
4 5	Comparison of the Two Models	50
5	CONCLUSION	54
	References	56

Nomenclature

$\alpha, \alpha_1, \alpha_2, \alpha_3$	Thermal diffusivity
c, c_1, c_2, c_3	Specific heat capacity
CEF	Concenterated energy flux
h	Clad thickness
l	Normalising length variable
L	heat propagation length
L_m	Heat of fusion of clad
q, q_0	Power density
s	Depth of melt
$S\epsilon$	absorbtion length
r_0	Laser beam radius
r_n	Nonuniformity in spatial distribution of Laser beam
t, t_1, t_2	Interaction time
T, T_1, T_2, T_3	Temperature
T_m	Melting temperature of clad
z	Cartesian coordinate
$\rho, \rho_1, \rho_2, \rho_3$	Density
θ_1, θ_2	Normalised temperature
λ_1, λ_2	Thermal conductivity
η	Normalised clad height
τ	Normalised interaction time
$\Delta\epsilon$	Normalised grid interval in z direction
$\Delta\tau$	Normalised time interval

Chapter 1

INTRODUCTION

Clad - metal composites having a number of valuable, partly unique properties have assumed ever increasing importance in modern engineering. Individual metals and alloys can not satisfy any more the ever increasing stringent, complex and often contrasting demands that materials have to meet in regard to strength, corrosion, wear, and/or heat resistance, electrical and thermal properties etc. Clad metal composites can be designed to satisfy different combination of desired properties. They can also be used as substitutes for more expensive alloys. The saving of scarce materials, cost reduction are among the other benefits that are incurred. Conventional methods of producing clad composites are roll bonding, extrusion, diffusion bonding and powder metallurgy routes. These methods use heat and pressure to obtain a sound interfacial diffusion bond. These methods require controlled atmosphere and take a long time and thus reducing the productivity. Experiments performed on laser cladding by V M Weerasinghe and W M Steen [1], Y Liu et al [2, 3], G Coquerelle, M Collin, J L Fachinetti [4], W Cerri et al [5], J Com-Nougue and E Kerrand [6], J Singh and J Mazumder [7], R M Machintyre [8], G Abbas and D R F West [9], Ming-Chang Jeng et al [10], V M Weerasinghe, W M Steen, and D R F West [11], S J Mathews [12], E Lugscheider, et al

[13], Ya D Kogan [14], show that laser is a powerful tool for cladding. Laser cladding is a process where interfacial fusion bond is achieved. This fusion bond is stronger than the diffusion bond. The time for cladding with laser is much lower than that of other methods and the atmosphere control is generally not required.

The main feature of a concentrated energy flux such as laser is its ability to deliver high power per unit area (10^2 – 10^4 W/mm²) to local regions on a workpiece and thus rapidly change the target temperature. Recent advances in laser technology have drawn considerable interest in using lasers for manufacturing. Laser technology not only makes manufacturing process simpler and more economical but also provides a unique way of modifying surface chemistry and structure of materials. Experimental studies confirm that the CEF can be a very useful tool in many potential applications involving surface hardening, surface cladding, welding, cutting, surface alloying and shock hardening. However, for its use to be consolidated it is necessary to predict how it would work in novel situations and novel materials. In understanding how it works, the experimenter is faced with a multiparameter problem which is difficult to solve without extensive factorial experimentation. The principal variables are the substrate thermal and optical properties, the laser power, power distribution and interaction time. Alternatively, an assumed physical picture of the process can be mathematically modeled and the model's result compared to experimental result to prove the model's validity and thus by inference the physical model.

A model capable of predicting experimental result means that previously unmeasurable parameters can be estimated. In metal cladding the most important data are (1) the thermal cycle in each location in the fusion and heat affected zone which defines the extent of any phase change, (2) the peak temperature distribution and (3) the cooling rates which would affect the formation of metastable structures such as martensite. Without a mathematical model

these values are very difficult to obtain

The objective of the present work is to model the surface cladding process, where the clad metal powder of uniform thickness is placed over the substrate and is irradiated with a stationary laser source so that the clad melts completely and forms a strong metallurgical bond with the substrate. The model should predict the melt boundary velocity, the peak temperature at all points and the temperature distribution. Uniform, high beam diameter, high beam intensity laser cladding process is modeled in one dimensional approximation by considering the nonlinear Stefan condition at the moving melt boundary. Since the exact turbulent behaviour of the melt is not known, the two extreme cases i.e. complete turbulence and no turbulence are considered. The temperature distribution during preheating and the preheating time are obtained from the Laplace transform solution of the governing one dimensional heat equations and boundary conditions. The temperature distribution during melting and the melting time are obtained by solving the one dimensional heat equations along with the boundary conditions and the energy balance equation by Crank - Nicholson finite difference method. Cladding of nickel and stainless steel over C - 45 steel at clad heights of 0.2 mm, 0.5 mm and 1 mm and at various power densities are considered for parametric study.

Chapter 2

LITERATURE REVIEW

2.1 Laser Material Interaction

When the laser falls on a target surface, part of the energy flux is reflected and a part is absorbed in a thin layer. The energy of absorbed light is given up to an electron gas via the triple collision of an electron, a photon and for example a lattice defect, which as revealed by calculation [15], is a necessary condition for fulfilling the law of conservation of momentum. The collision cause electron gas temperature to grow, but the lattice temperature generally remains invariable for a definite time, because of large difference in mass between electron and ion. Estimates disclose that the equalisation of electron gas temperature occurs for about 10^{-13} – 10^{-17} sec [15], which is much shorter than the time of energy transfer from electrons to ions.

The electron to ion energy transfer corresponds to electron photon interaction, which tend to equalize the temperature of the electron gas and the lattice. This process lasts around 10^{-11} sec, so that the notion of the heat source is valid after a dwell time of 10^{-9} to 10^{-10} sec.

When a triangular pulse interacts with a material, the maximum tem-

perature difference between the electrons and the lattice is given by [15]

$$(T_e - T_i)_{max} = \frac{2q}{\alpha \sqrt{\pi a \tau}} \quad (2.1)$$

where

T_e - electron gas temperature

T_i - ion temperature

q - flux density

α - electron lattice heat transfer coefficient

τ - light pulse length

a - thermal diffusivity

At $q = 10^1 \text{ W/mm}^2$ and $\tau = 10^{-3} \text{ s}$, $(T_e - T_i)_{max} < 1 \text{ K}$ at $q = 10^7 \text{ W/mm}^2$ and $\tau = 10^{-11} \text{ s}$, $(T_e - T_i)_{max} = 2000 \text{ K}$. In both cases, $\alpha = 6 \times 10^6 \text{ W/mm}^3 \text{ s}$ and $a = 100 \text{ mm}^2/\text{s}$. In laser beam material processing the pulse duration is much longer than 10^{-9} s and the power density is lower than 10^7 W/mm^2 so the notion of a heat source is justifiable. So the practical tasks concerned with CEF material heating at pulse duration in excess of 10^{-9} s and at power density lower than 10^7 W/mm^2 can in the main be considered on the basis of the mechanisms of common heat conduction, be it linear or nonlinear.

The heat produced by laser interaction is sufficient to cause change of phase and surface properties. With very high flux or longer heating times, evaporation will occur at the surface, often accompanied by the ejection of molten material. Still higher heating rates will produce gross vapourisation, the high velocity luminous plumb of vapour and particles and sometimes the propagation of potentially damaging stress waves. These can result in the emission from the surface of highly energetic ions and electrons and the formation of plasma plume that retreats from the surface at rates as high as 10^8 mm/s . The density of the plume may be so much that subsequent laser is absorbed by plasma plume rather than by surface. Applications using continuous lasers or involving welding or drilling of bulk materials generally require heat fluxes that are well below those that cause the formation of plasma.

2.2 Uniqueness of laser source

Interest in laser as a processing tool is as a result of it's uniqueness as a source of heat

- 1 The optical energy is converted into heat in a shallow region. The absorption depth may be the order of 20 nm
- 2 The high spatial coherence of laser beams allow focussing the beam to small spot of high optical intensity ($10^4 - 10^8$) W/mm^2 . This allows heating the material on a very fine spatial scale bringing the temperature of the heated material in a very short time. The thermal penetration depth is small and this property combined to small optical penetration makes laser heating primarily a surface phenomenon
- 3 The laser can be used without any physical contact with the work piece, thereby minimising possible contamination
- 4 Laser beams are easily modulated electronically. This allows interfacing the laser into complex computer controlled processes

The ability to effectively exploit these characteristics is enhanced by the availability of a number of different types of laser that are suitable for material processing. The choice of a laser depends on the particular application and the material to be processed. More than one type of laser will offer the combination of parameters necessary to do a job, and a decision to use a particular laser will be made on the basis of cost, availability of equipment and compatibility with other aspects of the fabrication sequence. The most commonly used lasers are pulsed ruby and Nd-glass, and pulsed and continuous CO_2 lasers

2.3 Laser Cladding

Achievement of a sound interfacial fusion bond is the main aim of laser cladding process. Laser cladding offers some unique advantages

- Controlled dilution level
- Localised heating which reduces thermal distortion
- Controlled shape
- Good thermal bonding
- Fine quench microstructures

These advantages usually lead to fundamental economic advantage over competing processes due to reduced after machining costs, and reduced product rejection due to unacceptable distortion. Added to these advantages are the improved metallurgy of the clad layer due to its moderately rapid quench and its ease of application since the process can be a noncontact one.

2.3.1 Methods of Laser Cladding

Laser cladding can be achieved in the following ways. The simplest way is to preplace the metal powder over the substrate with or without the help of a binder and expose to a laser source so that the powder melts completely and forms a strong fusion bond with the substrate (fig 2.1). The laser source can be moving or stationary. In order to cover areas considerably larger than the diameter of the laser beam, successive partially overlapping passes are deposited with a moving laser source. The other way is to inject powder particles by pneumatic powder delivery system into the molten pool produced by the laser beam (fig 2.2).

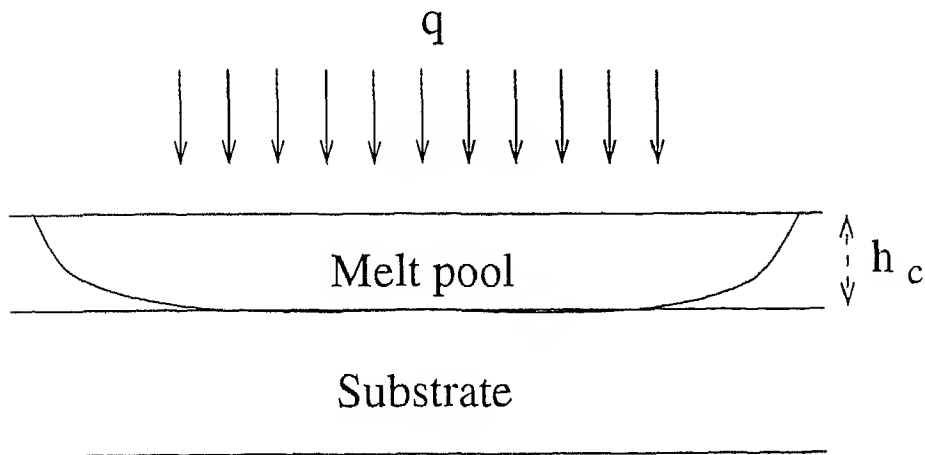


Figure 2.1 Laser cladding with preplaced powder

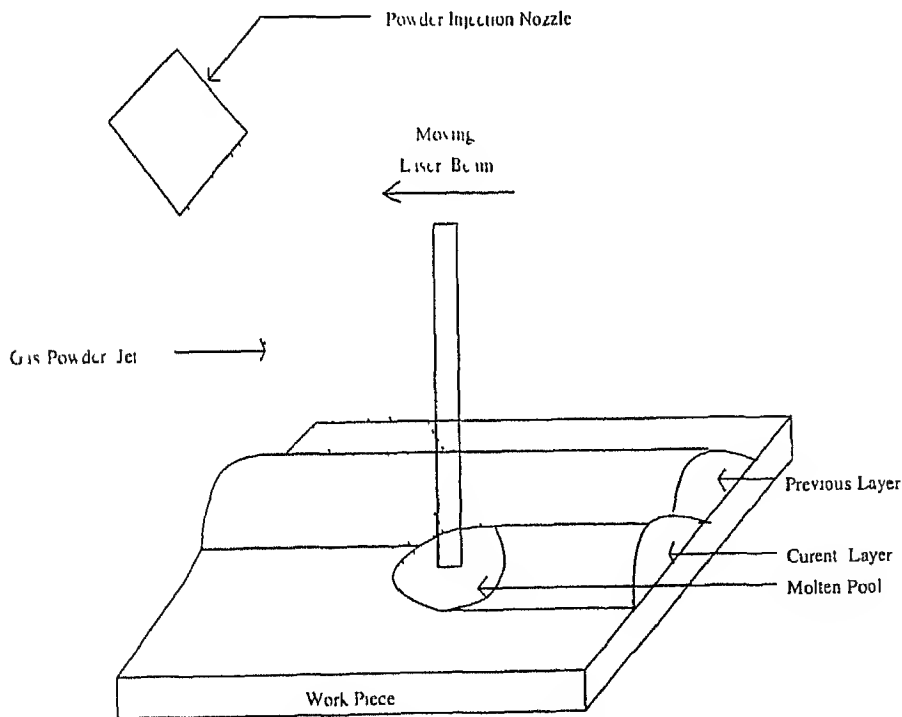


Figure 2.2 Laser cladding with pneumatic powder delivery

2.3.2 Clad substrate combination

Selection of a clad-substrate combination mainly depends on its end use. Most metal combinations can be clad provided the clad material doesn't have a sig-

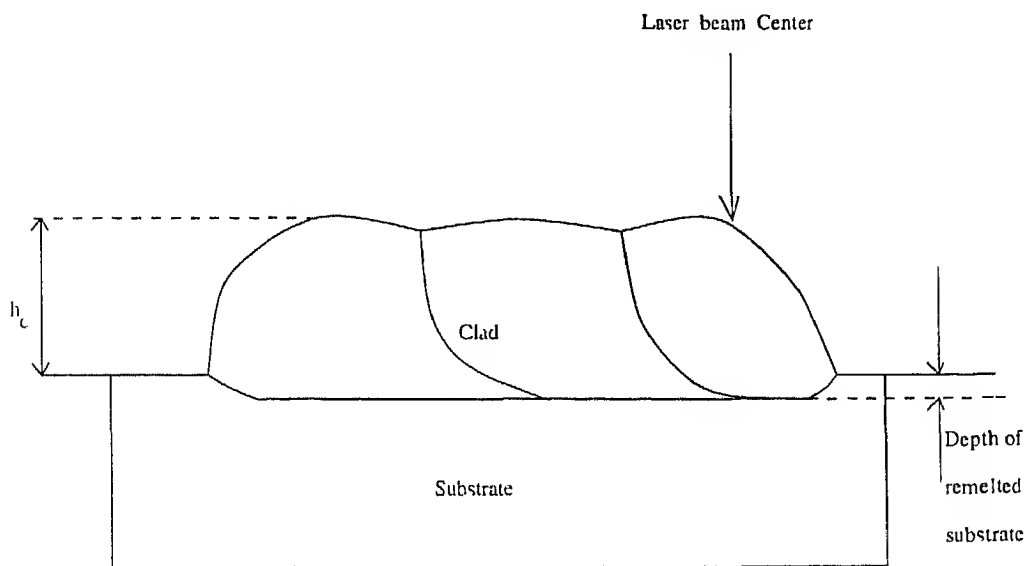


Figure 2.3 Laser clad

significantly higher melting point than the substrate [1]. The mixed solidification direction in these cases lead to interface porosity. The brittle compound formation at the interface must be avoided. The clad and substrate material should have sufficient ductility to compensate for thermal stresses [1, 2].

2.3.3 Experimental Results

V. M. Weerasinghe and W. M. Steen [1] obtained very good results for cladding 316 stainless steel on EN 3 mild steel, Stellite on mild steel, Stellite on tool steel (TiC), and stainless steel on mild steel, with a moving laser beam and pneumatic powder delivery system. Y. Liu, J. Mazumder and K. Shibata [2] were successful in cladding bronze over AA333 Al alloy in spite of the significantly higher melting temperature of bronze (1300 K) than Al alloy (800 K), with a moving laser beam and pneumatic powder delivery system. Y. Liu et al. [3] obtained good results for cladding Ni over AA333 Al alloy with Cu as the intermediate layer, with a moving laser beam and pneumatic powder delivery system. J. Singh and J. Mazumder [7] obtained excellent wear properties

for laser clad Cr, Mn, and C over AISI 1016 steel G Coquerelle et al [4] obtained good results for cladding Cobalt and nickel stellite on the edge of turbine blades W Ceiri et al [5] obtained hard, and wear resistant Fe-Cr-Al-Y alloy + TiC or WC clad over AISI 310 stainless steel using a stationary Gaussian source and pneumatic powder delivery system J Com-Nougue and E Kerand [6] obtained good clad characteristics for cladding Co-Cr alloy over 12% Cr steel using a 3 KW laser, moving laser beam and pneumatic powder delivery system J Singh and J Mazumder [7] developed in situ Ni-Cr-Al-Hf alloy over AISI 1016 steel using a 10 kW laser and pneumatic powder delivery R M MacIntyre [8] was successful in laser hard-surfacing of turbine blade shroud interlocks using a 2 KW CO_2 laser moving carriage and pneumatic powder delivery system G Abbas and D R F West [9] produced hard and wear resistant alloy and composite clad layers of SiC and Stellite on En 3b mild steel using a 2 KW CW CO_2 laser, moving laser beam, and pneumatic powder delivery Ming-Chang Jeng et al [10] investigated the wear properties and the wear mechanisms of stellite-6 powder clad over AISI 1020 steel A 2.5 KW CO_2 laser, pneumatic powder delivery and moving laser beam was used V M Weerasinghe et al [11] clad 316L stainless steel over mild steel using a 2 KW CO_2 laser, moving substrate and pneumatic powder delivery S J Mathews [12] investigated laser fusing of preplaced powder paste as viable hardfacing method A variety of stellite powders were clad over steel with a 1.2 KW CO_2 laser with moving beam Ya D Kogan [14] analysed laser surface alloying of iron, structural and tool steels and Al, Cu, and Ti and their alloys E Lugscheider et al [13] obtained good coatings of Co-Cr-W-B-Si and Co-Ni-Cr-B-Si hardfacings using a preplaced powder paste and moving substrate

The effect of the process parameters, laser power, laser beam diameter, traverse speed, powder feed rate and powder size and shape on the dependent variables of clad shape, dilution, porosity, cracking, surface finish, substrate

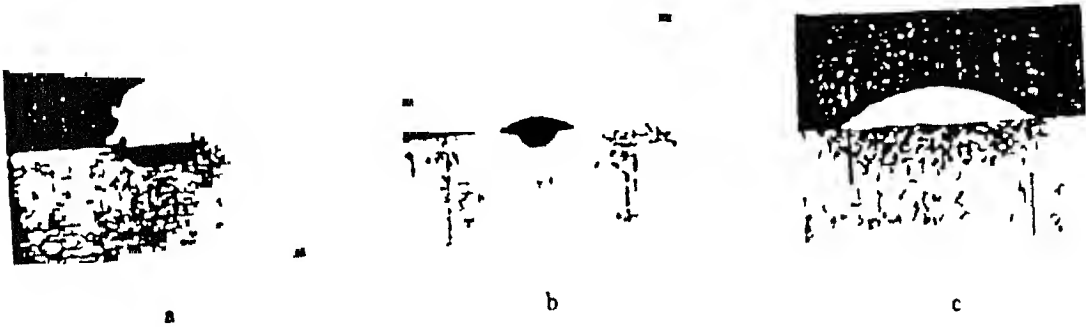


Fig 2.4 Three basic clad section profiles
Stainless steel clad over steel

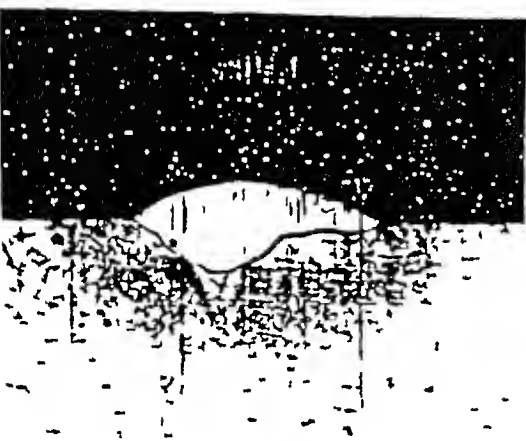
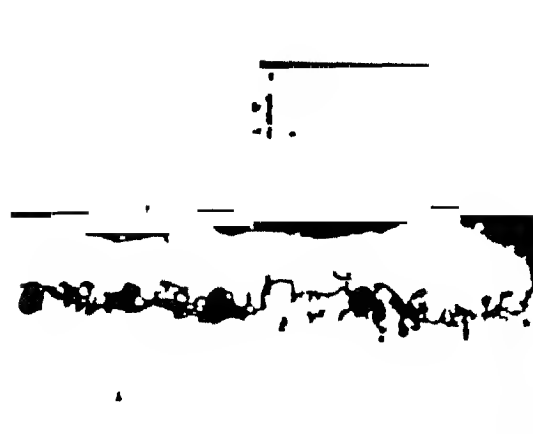


Fig 2.5 Effect of unsymmetric beam
distribution



Fig 2.6 Interrun porosity
s/s clad over m/s



distortion, cladding rate from experimental results are discussed below

(a) Clad shape

V M Weerasinghe and W M Steen [1] observed three basic cross section profiles of single tracks as shown in fig 2.4. Profile 2.4 c is the preferred section for overlapping tracks to cover an area. At higher powder feed rates or lower power densities profile as in fig 2.4 a is produced while at lower powder feed rates or higher power densities profile as in fig 2.4 b is produced. For a given traverse speed and powder flow, there is an optimum spot diameter for maximizing the clad rate. Defocused beams produce profile as shown in fig 2.5.

(b) Dilution

For a given specific energy the powder mass flow controls the level of dilution [1]. Dilution is independent of cladding speed for cladding 316 stainless steel over mild steel [1]. Traverse speeds lower than 8.6 mm/s tend to produce large dilution for cladding bronze over AA333 Al alloy [2]. A higher laser power increased interface region and dilution [2]. Thinner clad tracks lead to large dilution [2]. Increasing the helium flow reduced the dilution but, a large helium flow increased porosity [2]. Increase in traverse speed increased dilution and decreased deposition rate in hardfacing with a preplaced paste of Ni-Cr-B-Si clad [13]. The hardness of the cladding was influenced by the degree of dilution and the dilution increased with increase of traverse speed [13].

(c) Porosity

Porosity in laser clad may be caused by one or a combination of the following: cavities between tracks (interrun porosity, fig 2.6), solidification cavities, gas evolution. Interrun porosity occurred when two tracks of section profile similar to fig 2.4 a were laid side by side with insufficient overlap [1]. It could be totally eliminated by operating in such a way in fig 2.4 c. It can also be eliminated by ultrasonically vibrating the substrate during laser cladding or by angling

the powder feed around 10° to the line of the clad track. Solidification cavities occur at or near the interface between the cladding and the substrate if the clad has a significantly higher melting point than the substrate [2, 1]. Inter-run porosity occurs with high aspect ratio and large overlapping percentage [2] for cladding bronze over AA333 Al alloy. The best overlapping clads were achieved for the above case with a combination of aspect ratio 3 to 3.7 and overlap percentage 40-55.

(d) Cracking

Cracking occurs due to tensile solidification stresses which result from differential thermal expansion in the steep thermal gradients associated with laser processing (fig 2.7). These tensile stresses result in cracking of nonductile clad layers or layers with stress raisers due usually to porosity. Thus cracking is observed on Fe/B but not on stainless steel or stellite [1]. The thermal stresses developed for a cold substrate with no relaxation is given as

$$\sigma = \frac{E_s E_c}{E_c + E_s} \beta \Delta T \quad (2.2)$$

where

E_s - Young's modulus of substrate

E_c - Young's modulus of clad

β - thermal expansion coefficient

ΔT - temperature change

Cracking of difficult systems can be eliminated by preheating [1, 2, 3]. The safe power input corresponding to a certain preheating temperature for cladding of Ni over Al alloys is estimated by [3]

$$P_i - P_f < (850 - T_h) C_p \quad (2.3)$$

where

P_i - total power

P_f - power needed for fusion of Ni alloy

T_h - preheat temperature

C_p - specific heat capacity

Interdendritic cracking was observed in clad layer produced at high cladding speeds and with high power densities [11]. 180° bend tests on stainless steel clad layers over En3 mild steel revealed only vertical cracks through clad layers or none at all. There were no examples of delaminating or interfacial cracks [1]. On stellite/monel, monel/steel, bronze/steel clads a side blow with a chisel, very rarely removed the clad at the interface.

(e) Surface finish

The degree of overlap of adjacent tracks and the section profile of each track govern the surface finish of the clad layer. With sufficient overlap (50 - 60 %) a good surface finish can be obtained (fig 2.8). The surface undulations caused by overlapping were typically less than 0.04 mm in contrast to 0.15 mm typical of arc weld overlays for 316L stainless steel over mild steel [1, 11].

(f) Homogeneity of clad layer

Heavily diluted layers showed an almost uniform composition, suggesting that there is considerable stirring in the pool. The solidification mechanism is usually dendritic along the steepest thermal gradients. A drastic change of composition is observed in the interface region which is less than 0.1 mm [2, 1].

(g) Substrate distortion

Measurements on the HAZ indicate that there is minimal thermal penetration of the substrate and hence minimal distortion. However there is some distortion due to contractural stress set up by the solidifying clad layer.

(h) Cladding rate and clad thickness

Figs 2.9 and 2.10 show the relationship between the cladding speed, and the width and the height of a single track for a fixed beam diameter, laser power, and powder flow conditions [1]. By varying the power, or the beam diameter it was shown that the edge of the cladding has a constant power density.

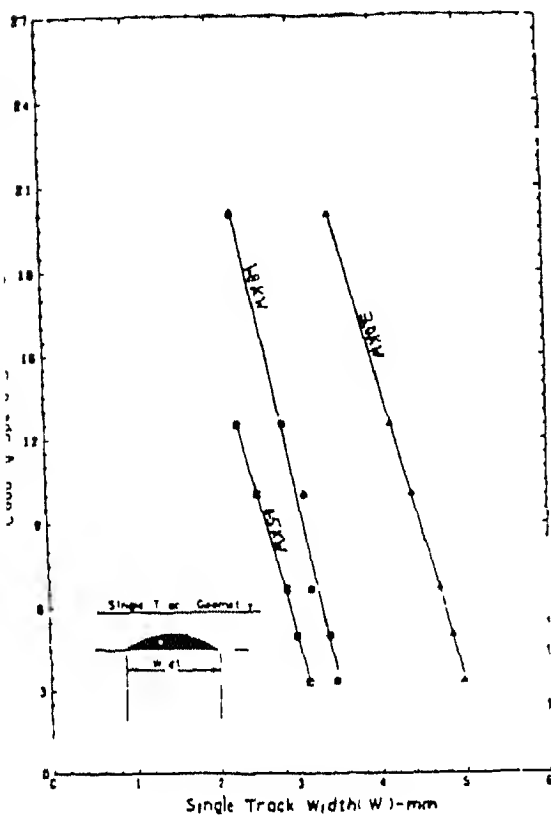


Fig 2.9 Effect of cladding speed on single track width

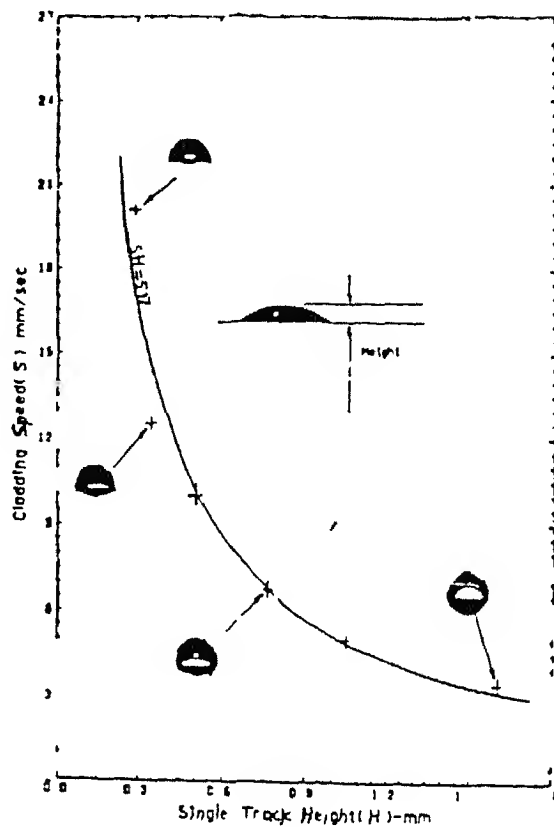
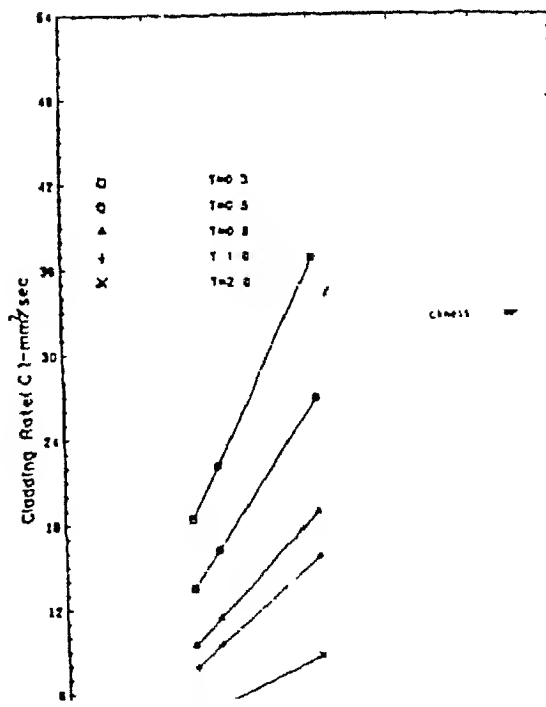
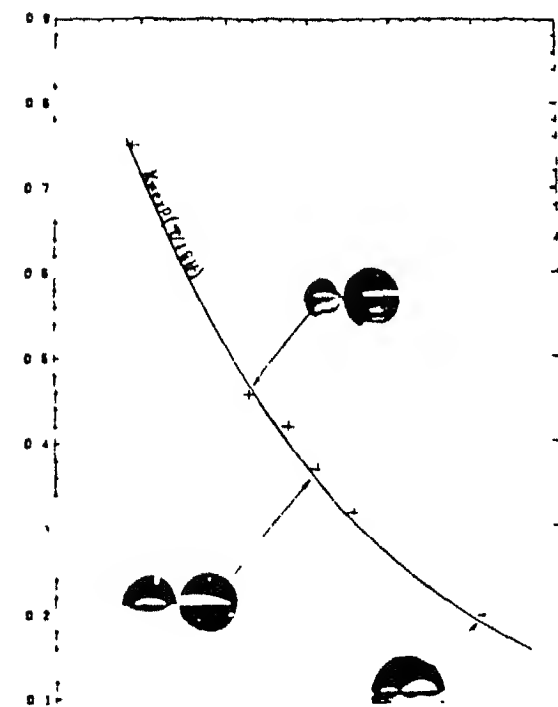


Fig 2.10 Effect of cladding speed on single track height



The effect of the overlap on the minimum clad thickness is shown in fig 2.11. From fig 2.8, 2.10, 2.11 all at constant laser power, beam diameter, and powder flow conditions, the following relationships were drawn [1]

$$S = a - bw \quad \text{fig 2.9} \quad (2.4)$$

$$k = e^{\frac{-T}{1.8H}} \quad \text{fig 2.11} \quad (2.5)$$

$$SH = d \quad \text{fig 2.10} \quad (2.6)$$

$$C = kwS \quad (2.7)$$

where

- S - cladding speed (mm/s)
- w - single track width (mm)
- H - single track height (mm)
- T - multiple track minimum clad thickness (mm)
- k - overlap factor
- C - coverage rate (mm^2/s)
- a, b, c, d - constants

From the above equations the cladding rate as a function of speed and thickness can be obtained. By differentiating this expression the speed giving the maximum cladding rate can be found and hence the optimum overlap required.

For cladding of bronze over AA333 Al alloy, a rough estimation of the clad thickness is given as [2]

$$\text{net clad height} \approx 0.64 P_f \quad (2.8)$$

or

$$0.75 w t S_p S_w = 0.64 P_f \quad (2.9)$$

where

- w - width of the clad (mm)
- t - thickness of the clad (mm)
- S_p - traverse speed (mm/s)
- S_w - specific weight (g/mm^3)
- 0.64 - powder utilisation coefficient
- P_f - powder feed rate (g/s)

Here $0.75 \times w \times t$ gives a rough estimate of the cross sectional area of the clad track. So a higher powder feed rate will produce a thicker clad track. For a given substrate condition and helium flow there is a minimum clad thickness for which good clads can be made. Using substrate with polished surface effectively reduced the minimum clad thickness. The optimised processing parameters for cladding Ni alloy on Cu plate and Al substrate with bronze intermediate layer are summarized below

substrate	Mirror	Power KW	Speed mm/s	Powder feed rate (g/s)	Preheat temp (K)
Cu	Oscillating	6.09	15.5	0.6833	673
Bronze	Oscillating	2.9	9.3	0.45	673

A good compact cobalt based alloy clad over 12% Cr steel is obtained at travelling speeds from 5 mm/s to 11.67 mm/s and corresponding to three different distance between successive passes, namely, 1.25, 1.62 and 2 mm. The thickest coating achieved in this case is 0.96 mm at a 5 mm/s speed. An increase in the overlapping rate lead to an increase in the clad thickness and values higher than 1.3 mm were reported [6].

(1) Microstructure

Laser cladding leads to extremely fine microstructure due to high cooling rate (fig 2.13) [2, 7]. There is a HAZ in the overlapping clads, and in the HAZ there is no macroscopic segregation [2]. Uniform and fine undissolved Hf in the Ni matrix could be achieved by cladding with pneumatic powder delivery [7]. Laser hardfacing of turbine blades produces a higher quality hard-faced deposit [8]. Microstructural studies showed excellent bonding of the SiC clad layer to stellite substrate [9]. The SiC particles tend to segregate to the upper region of the clad as a result of its low density compared to stellite. The lower region that contained the partially dissolved SiC particles is referred to as the stellite matrix of the clad. Slightly more porosity is found in the composite

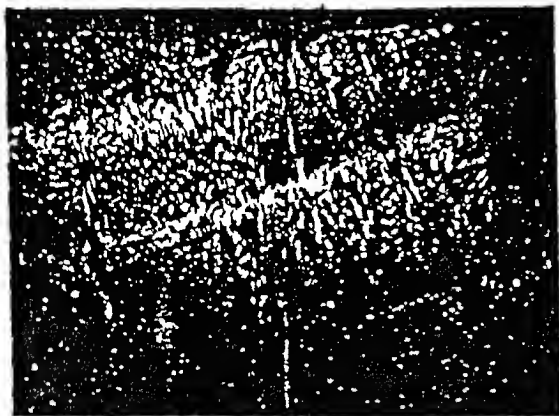


Fig. 2.13 Fine dendritic microstructure
of 316 stainless steel clad

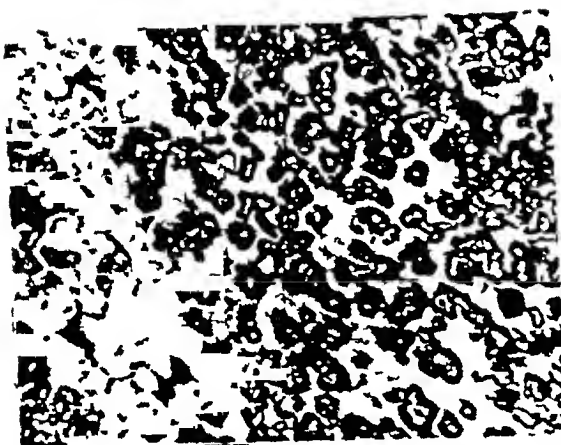
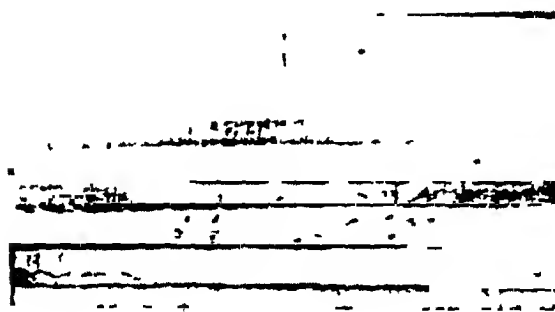


Fig. 2.14 TiC particles in a stainless
steel 316 clad matrix



than in stellite. The matrix of the clad showed a fairly uniform dendritic structure typical of stellite. Large densities were found with lower traverse speeds due to high percentage of stellite.

The microstructure of Co based alloy clad over steel showed equiaxial structures surrounded by dendritic structures near the surface. Some porosities and impurities were found in the overlapping area near the interface.

2.4 Mathematical Models

The absorption of radiation and heating of the body can be treated in the unidimensional approximation when [16]

$$r_0 \geq r_n \gg \max\{\varepsilon, L\}$$

where

r_0 -radius of the laser beam

r_n -nonuniformity of the spatial distribution of the laser beam

ε -absorption length

$L = \sqrt{at}$ -heat propagation length

This condition is obviously not met in all cases of interaction of the laser with materials, but at large beam radius and at initial stages of heating, both by pulsed and continuous sources can be treated in unidimensional model.

To date, few models for laser cladding have been proposed. A. Kar and J. Mazumdar [17] modeled in one dimensional approximation the laser cladding process where the substrate material is moved at constant speed while the clad material is poured onto it using a pneumatic powder delivery system and melted simultaneously with a uniform laser beam as shown in fig 2.16. The

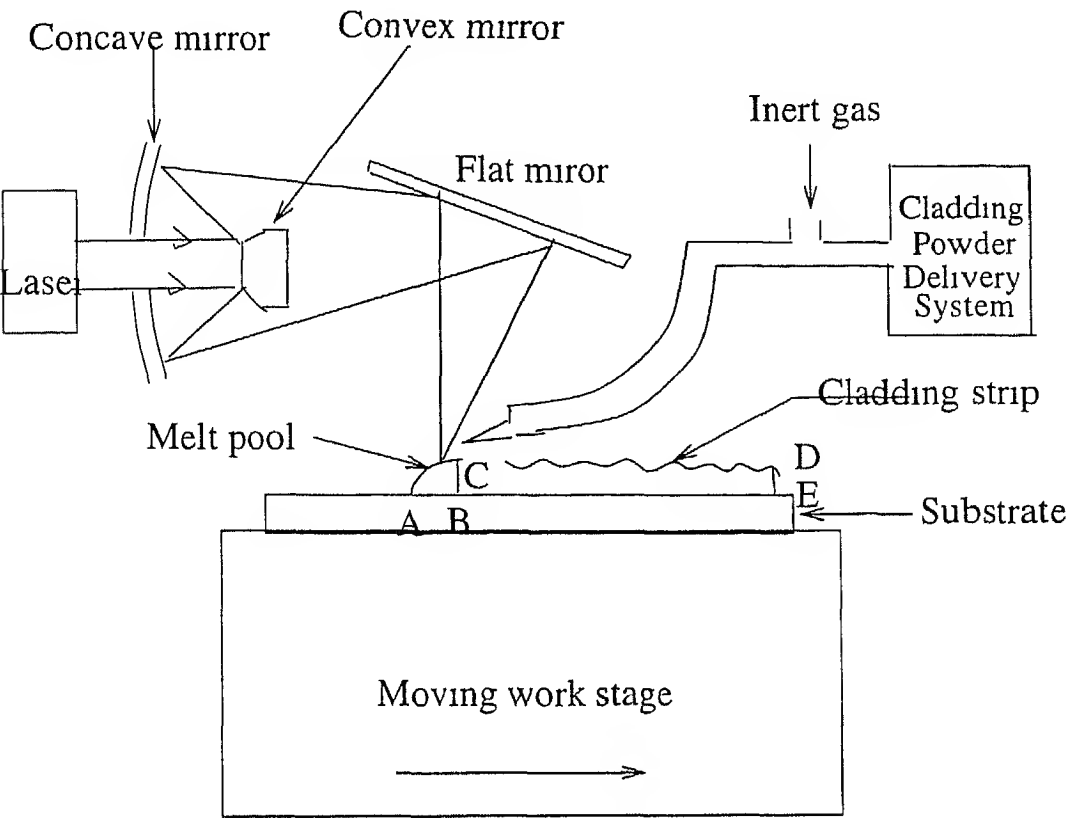


Figure 2 16 Laser cladding with pneumatic powder delivery

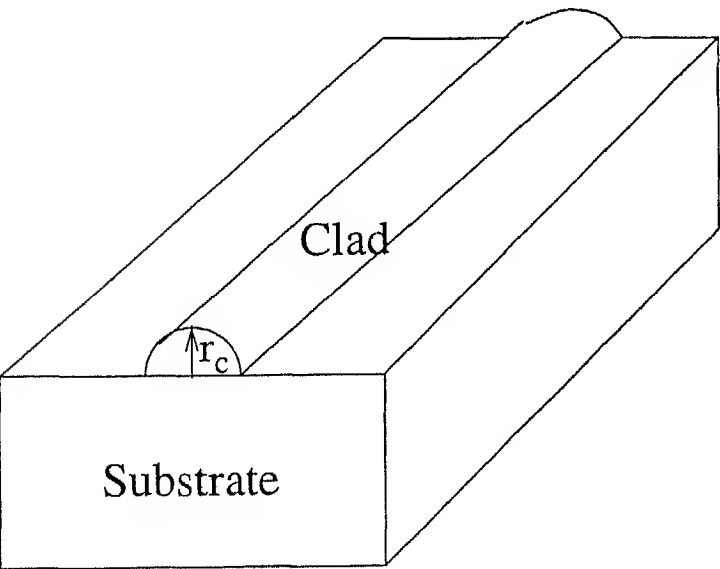


Figure 2 17 Semi-Cylindrical Laser clad

authors were concerned with the heat and mass transfer in the cladding melt ABCA to model the extended solid solution during laser cladding. To carry out one dimensional heat transfer calculations they assumed that the pool extends upto infinity along AB. Due to this assumption, cladding melt solidifies Along AB and this moves upwards along the direction of BC. The Stefan condition is considered at the moving boundary. The strip of cladding is assumed to be semi-cylindrical in shape (fig 2.17). The freezing front is assumed to be planar due to small size of dendrites. Stefan condition is used at the melt boundary. The governing heat equations and boundary conditions are solved using the integral transform technique. The cladding is assumed to melt almost instantaneously as soon as it is exposed the laser beam to reach a uniform temperature T_2 . Thus yields the following expression for T_2 ,

$$T_2 = T_1 + \frac{1}{C_p} \left[\frac{2pf}{\pi r_c^2 v} - L \right] \quad (2.10)$$

where

T_1 - ambient temperature

C_p - average specific heat of cladding material

p - laser power

f - fraction of laser power absorbed by the cladding material

r_c - radius of the clad strip

v - speed of the workpiece

L - latent heat of fusion of the clad material

The results of the model were compared with experimental data. Laser cladding was performed on Ni substrate with a mixture of Ni-Hf powder of nominal composition 74% Ni and 26% Hf by weight. The laser power, laser beam diameter, and the interaction time used were 5 KW, 3 mm and 1.44 s. EPMA and STEM analysis showed that the concentration of Hf obtained in the nickel matrix is in excess of that predicted by the equilibrium phase diagram. The experimental results show that 3.58 - 6.5 wt% of Hf in the Ni matrix.

The theoretical result predicted by the model is 7.15 wt% Hf in the Ni-Hf alloy. This model was used to study the effect of laser power, interaction time, cladding thickness, cladding powder delivery rate on the composition of Hf in the Ni matrix. The concentration of Hf was found to increase with increase of cladding thickness for a given speed of workpiece and laser power. However, it would be erroneous to conclude that one can enrich the solid phase with solute to any concentration by increasing the cladding thickness indefinitely for a given laser power and a given speed of the workpiece. There is a critical value of the cladding thickness of which T_2 becomes equal to the melting point of the cladding. If the cladding thickness is greater than the critical value then there will be some unmelted powder between the substrate and the cladding melt and hence the substrate will not be clad. It is found that more laser energy is required to obtain an alloy of a given composition at a higher powder delivery rate than at a lower powder delivery rate.

P.H. Steen et al [18] developed a model for predicting melt depth for a single layer material based on a two dimensional conduction balance equation. Uniform source moving at a constant speed is used. The predicted melt depth is given as

$$\frac{d_m}{d} = \left(\frac{4}{\Pi} \right)^{\frac{1}{2}} P^{\frac{1}{2}} - (\theta_m - 1) Q^{-1} \quad (2.11)$$

where

d - laser beam width in the direction of beam motion

$p = \frac{Ud}{\alpha_s}$ - nondimensionalised scanning speed

U - scanning speed

α_s - thermal diffusivity of substrate

$\theta_m = \frac{T_m}{T_\infty}$ - scaled melting temperature

T_m - melting point of substrate

T_∞ - farfield temperature

$Q = \frac{qd}{\lambda_s T_\infty}$ - nondimensionalised power density

q - absorbed power density

λ_s - thermal conductivity of the substrate

The melt thermal properties and the latent heat of fusion are not considered.

This is valid for melting shallow region.

Laser melting of a single plate with a moving Gaussian source has been modeled by S. Kou and Y. H. Wang [19] considering three-dimensional convection. The equation of motion, equation of continuity, and equation of energy are solved by finite difference method. They obtained excellent agreement with the experimental results performed on 6063 aluminium sheets of $229\text{ mm} \times 152\text{ mm} \times 3.2\text{ mm}$ at 1.3 KW laser power. This is melting of a single plate and can not be treated as a cladding case.

M. Picasso, et al., [20] modeled cladding with a gaussian moving source and pneumatic powder delivery system in three dimension (fig 2.2). The powder is assumed to be predeposited on the substrate and the power absorbed by the workpiece, P_w , is used to remelt the clad. The attenuation of the laser beam by the powder particles and the surface reflection are considered. The heat of fusion is neglected. Simple heat equations in three dimension are solved by Laplace transform method. The temperature T within the material, for Gaussian distribution is given as

$$T(x, y, z) = T_{amb} + \frac{P_w}{\Pi^{\frac{3}{2}} k r_l} \int_0^\infty f(x, y, z, s) ds \quad (2.12)$$

where

$$f(x, y, z, s) = \frac{1}{1+s^2} \exp \left[\frac{-s^2}{1+s^2} \left[\left(\frac{x}{r_l} - \frac{a r_l}{2s^2} \right)^2 + \left(\frac{y}{r_l} \right)^2 \right] - s^2 \left(\frac{z}{r_l} \right)^2 \right]$$

- T_{amb} - ambient temperature
- P_w - absorbed laser power
- $a = \frac{\rho c v_l}{2k}$
- ρ - density of clad material
- c - specific heat of clad
- v_l - laser beam velocity
- k - thermal conductivity of clad
- r_l - laser beam radius

The temperature T within the material, for cylindrical distribution of laser beam is given as

$$T(r, y, z) = T_{amb} + \frac{P_w}{2\Pi^2 k r_l^2} \int_0^{2\Pi} \int_0^{r_l} \frac{1}{R} e^{a(x-r\cos\theta-R)} r dr d\theta \quad (2.13)$$

where

$$R^2 = (x - r\cos\theta)^2 + (y - r\sin\theta)^2 + z^2$$

The melt boundary corresponds to the region which is at the clad melting point

Experiments were carried out with the following data

Laser power	1360 W
Injection angle of nozzle	55°
Powder velocity	2500 mm/s
Average powder radius	0.0025 mm
Clad material	Stellite -6
Substrate	mild steel (0.1% C)
k	0.01 W/mm K
ρc	0.0035 J/mm ³ K
T_f	1573 K

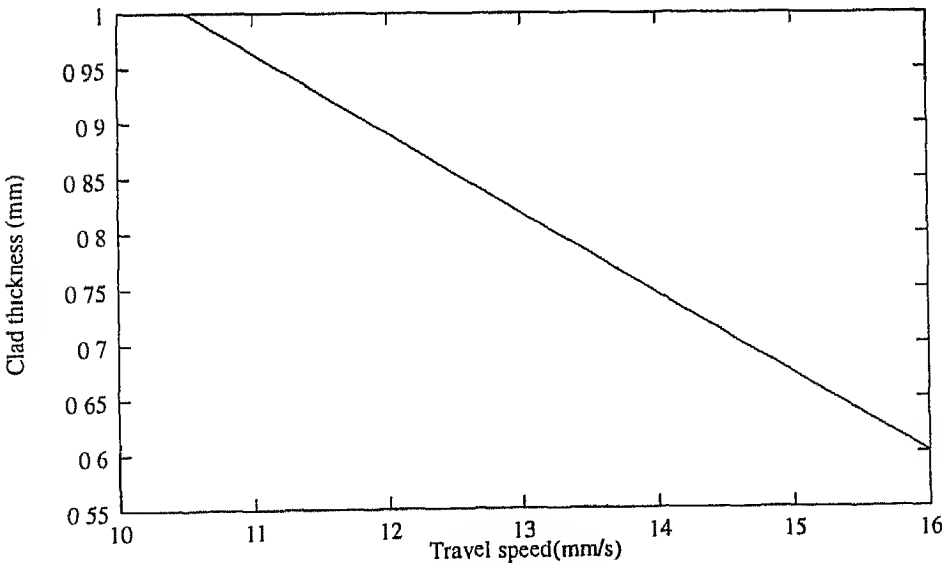


Figure 2.6 Travel speed vs Clad thickness

The numerical results (fig 2.6) and experimental results are in good agreement

The models discussed above correspond to laser cladding with pneumatic

powder delivery. They are not valid for cladding with preplaced powder. Simple three dimensional models have the limitation of its inability to accommodate heat of fusion. Finite difference methods involve much computation and are complex. The present model is for preplaced powder technique and this accommodates heat of fusion. This model uses less computational intensive finite difference method. But, this model assumes one dimensional approximation, which is valid for large beam diameter and small interaction time.

Chapter 3

ONE DIMENSIONAL MODEL FOR LASER CLADDING

3.1 Introduction

The simplest way of surface cladding with laser is, to preplace the clad powder over the substrate and then expose to a uniform, stationary laser beam is modeled. One dimensional heat transfer, which is valid for large beam diameter and high power density is considered. The turbulence occurring in the melt during melting and hence the melt thermal conductivity is not exactly known. Hence, modeling is done for the two extreme cases, complete turbulence and no turbulence. The actual heat transfer process occurring during laser heating are very complex with nonlinearities of thermal constants and anisotropic material properties. The laser source has changing spatial temporal characteristics. As done by many others [17, 20, 22] the following assumptions are made throughout this work

- Isotropic material
- Stable thermal conductivity, density, and specific heat

- No heat loss to surrounding by radiation
- Ideal thermal contact at two phase interfaces
- Complete absorption of the incident beam
- Planar freezing front
- All heat is absorbed at the surface only
- The clad material has a unique melting point
- Substrate is semi-infinite

The anisotropic nature of the materials depend on a number of factors like, prior treatment, and it's spatial distribution can not be predicted. The thermal constants may vary to a considerable extent, but difficult to model. Owing to a small interaction time and a large heat flux coming in the heat loss to the surrounding can be neglected. Thermal resistance between powder clad and substrate is not exactly known. The power density considered for calculation is the actual power absorbed by the clad.

3.2 Turbulent melting

In this model the melt pool is assumed to be so turbulent that it has infinite thermal conductivity. Consider a uniform laser source heating the surface of a semi-infinite body over which the clad powder is preplaced to a uniform thickness. The rise in surface temperature is limited by the heat conduction into the material from hotter to colder metal and heat of fusion. When the surface is below the melting point the surface condition becomes

$$-\lambda_1 \frac{\partial T_1}{\partial z} = q_0 \quad (3.1)$$

When the surface reaches the melting point, liquid metal forms and the melt boundary moves with certain velocity $\frac{ds}{dt}$ into the clad. Now, according to this model, the laser effectively falls on the moving melt boundary. One condition

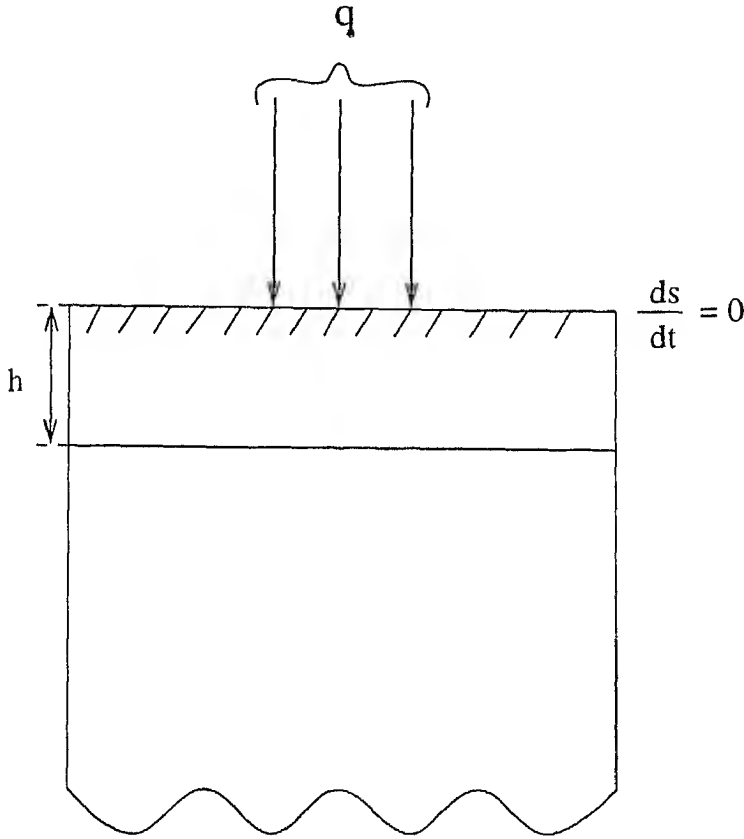


Figure 3.1 Preheating with uniform source

at the moving boundary $s(t)$ is that

$$T_1 = T_m \quad (3.2)$$

The other condition at the moving boundary is the Stefan condition, i.e.,

$$-\lambda_1 \frac{\partial T_1}{\partial z} = -\rho_1 L_m \frac{ds}{dt} + q_0 \quad (3.3)$$

The one-dimensional unsteady state heat conduction equation for the clad layer and the substrate are given below

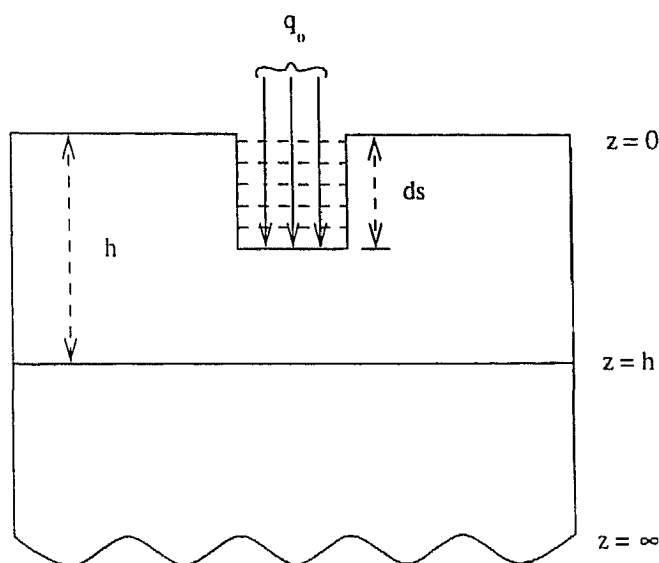


Figure 3.2 Turbulent melting with uniform source

At $s(t) < z < h$

$$\frac{\partial T_1}{\partial t} = a_1 \frac{\partial^2 T_1}{\partial z^2} \quad (3.4)$$

At $h < z < \infty$

$$\frac{\partial T_2}{\partial t} = a_2 \frac{\partial^2 T_2}{\partial z^2} \quad (3.5)$$

The clad-substrate contact, assumed to be ideal, results in the boundary conditions

At $z = h$

$$T_1 = T_2 \quad (3.6)$$

$$\lambda_1 \frac{\partial T_1}{\partial z} = \lambda_2 \frac{\partial T_2}{\partial z} \quad (3.7)$$

Temperature at $z = \infty$ remains constant

At $z = \infty$

$$T_2 = T_0 \quad (3.8)$$

Initial temperature of the clad and substrate is same throughout, (T_0)

At $t = 0$

$$T_1 = T_2 = T_0 \quad (3.9)$$

For numerical calculations instead of equation (3.3) a more convenient form can be obtained by considering the rate of change of heat in the material

$$\begin{aligned} \frac{d}{dt} \left[\int_0^h \rho_1 c_1 T_1(z, t) dz + \int_h^\infty \rho_2 c_2 T_2(z, t) dz \right] &= -\rho_1 c_1 T_m \frac{ds}{dt} + \rho_1 c_1 \int_{s(t)}^h \frac{\partial T_1}{\partial t} dz \\ &\quad + \rho_2 c_2 \int_h^\infty \frac{\partial T_2}{\partial t} dz \\ &= -\rho_1 c_1 T_m \frac{ds}{dt} + \lambda_1 \left[\frac{\partial T_1}{\partial z} \right]_s^h \\ &\quad + \lambda_2 \left[\frac{\partial T_2}{\partial z} \right]_h^\infty \\ &= -\rho_1 c_1 T_m \frac{ds}{dt} - \rho_1 L_m \frac{\partial ds}{\partial t} \\ &\quad + q(t) \end{aligned} \quad (3.10)$$

Integrating the above equation over any time interval (t_1, t_2) gives

$$\begin{aligned} \int_{t_1}^{t_2} q(t) dt &= \rho_1 c_1 \int_{s(t_2)}^h T_1(z, t_2) dz - \rho_1 c_1 \int_{s(t_1)}^h T_1(z, t_1) dz + \\ &\quad \rho_2 c_2 \int_{s(t_2)}^h T_2(z, t_2) dz - \rho_2 c_2 \int_{s(t_1)}^h T_2(z, t_1) dz + \\ &\quad \rho_1 (c_1 T_m + L_m) (s(t_2) - s(t_1)) \end{aligned} \quad (3.11)$$

When the surface is below the melting point, the equations and linear boundary conditions can be solved by Laplace Transform method to get the temperature distribution. The clad layer temperature distribution is given as,

$$T_1 = \frac{2q_0}{\lambda_1} \sqrt{a_1 t} \left[\sum_{n=0}^{\infty} g^{n+1} \operatorname{erfc} \left[\frac{2h(n+1) - x}{2\sqrt{a_1 t}} \right] + \sum_{n=0}^{\infty} g^n \operatorname{erfc} \left[\frac{2nh + x}{2\sqrt{a_1 t}} \right] \right] \quad (3.12)$$

The substrate temperature distribution is given by,

$$T_2 = \frac{2q_0}{\lambda_1}(1+g)\sqrt{a_1 t} \sum_{n=0}^{\infty} g^n \operatorname{erfc} \left[\frac{(2n+1)h + (x-h)\sqrt{\frac{a_1}{a_2}}}{2\sqrt{a_1 t}} \right] \quad (3.13)$$

where erfc is the integral of the complementary function

$$\begin{aligned} \operatorname{erf}(x) &= \frac{2}{\sqrt{\pi}} \int_0^x e^{-y^2} dy \\ \operatorname{erfc}(x) &= 1 - \operatorname{erf}(x) \\ \int_x^{\infty} \operatorname{erfc}(y) dy &= \frac{1}{\sqrt{\pi}} e^{-x^2} - x \operatorname{erfc}(x) \end{aligned}$$

When melting occurs, the formulated equations with nonlinear boundary condition can be solved by Crank-Nicholson implicit finite difference method. It is convenient to introduce the following normalised variables

$$\theta_1 = \frac{T_1 - T_0}{(T_m - T_0)} \quad (3.14)$$

$$\theta_2 = \frac{T_2 - T_0}{(T_m - T_0)} \quad (3.15)$$

$$l = \frac{a_1 \rho_1}{q_0} (c_1(T_m - T_0) + L_m) \quad (3.16)$$

$$\zeta = \frac{z}{l} \quad (3.17)$$

$$\psi = \frac{h}{l} \quad (3.18)$$

$$\varepsilon = \frac{s}{l} \quad (3.19)$$

$$\tau = \frac{a_1 t}{l^2} \quad (3.20)$$

Now, the boundary conditions and equations [3.2, 3.4–3.9, 3.11] after normalising using equations 3.14–3.20 are as below

At $\zeta = \varepsilon(t)$

$$\theta_1 = 1 \quad (3.21)$$

At $\varepsilon(t) < \zeta < \psi$

$$\frac{\partial \theta_1}{\partial \tau} = \frac{\partial^2 \theta_1}{\partial \zeta^2} \quad (3.22)$$

At $\zeta = \psi$

$$\theta_1 = \theta_2 \quad (3.23)$$

$$\frac{\partial \theta_1}{\partial \zeta} = \frac{\partial \theta_2}{\partial \zeta} \quad (3.24)$$

At $\psi < \zeta < \infty$

$$\frac{a_1}{a_2} \frac{\partial \theta_1}{\partial \tau} = \frac{\partial^2 \theta_1}{\partial \zeta^2} \quad (3.25)$$

At $\zeta = \infty$

$$\theta_2 = 0 \quad (3.26)$$

The energy balance equation becomes

$$\begin{aligned} \int_{\tau_1}^{\tau} \frac{q_0 l^2}{\alpha_1} d\tau &= \rho_1 c_1 (T_m - T_0) l \int_{\varepsilon(\tau_2)}^{\psi} \theta_1(\zeta, \tau_2) d\zeta - \\ &\quad \rho_1 c_1 (T_m - T_0) l \int_{\varepsilon(\tau_1)}^{\psi} \theta_1(\zeta, \tau_1) d\zeta + \\ &\quad \rho_2 c_2 (T_m - T_0) l \int_{\psi}^{\infty} \theta_2(\zeta, \tau_2) d\zeta - \\ &\quad \rho_2 c_2 (T_m - T_0) l \int_{\psi}^{\infty} \theta_2(\zeta, \tau_1) d\zeta - \\ &\quad \rho_1 l (c_1 (T_m - T_0) + L_m) (\varepsilon(\tau_2) - \varepsilon(\tau_1)) \end{aligned} \quad (3.27)$$

The normalised equations written in the Crank-Nicholson finite difference form are given below

At $\zeta = \varepsilon(t)$

$$\theta_1 = 1 \quad (3.28)$$

At $\varepsilon(t) < \zeta < \psi$

$$\frac{\theta_i^{n+1} - \theta_i^n}{\Delta \tau} = \frac{\theta_{i+1}^{n+1} - 2\theta_i^{n+1} + \theta_{i-1}^{n+1} + \theta_{i+1}^n - 2\theta_i^n + \theta_{i-1}^n}{2\Delta \zeta^2} \quad (3.29)$$

At $\zeta = \psi$

$$\lambda_1 \left[\frac{\theta_i^{n+1} - \theta_{i-1}^{n+1}}{\Delta \zeta} \right] = \lambda_2 \left[\frac{\theta_{i+1}^{n+1} - \theta_i^{n+1}}{\Delta \zeta} \right] \quad (3.30)$$

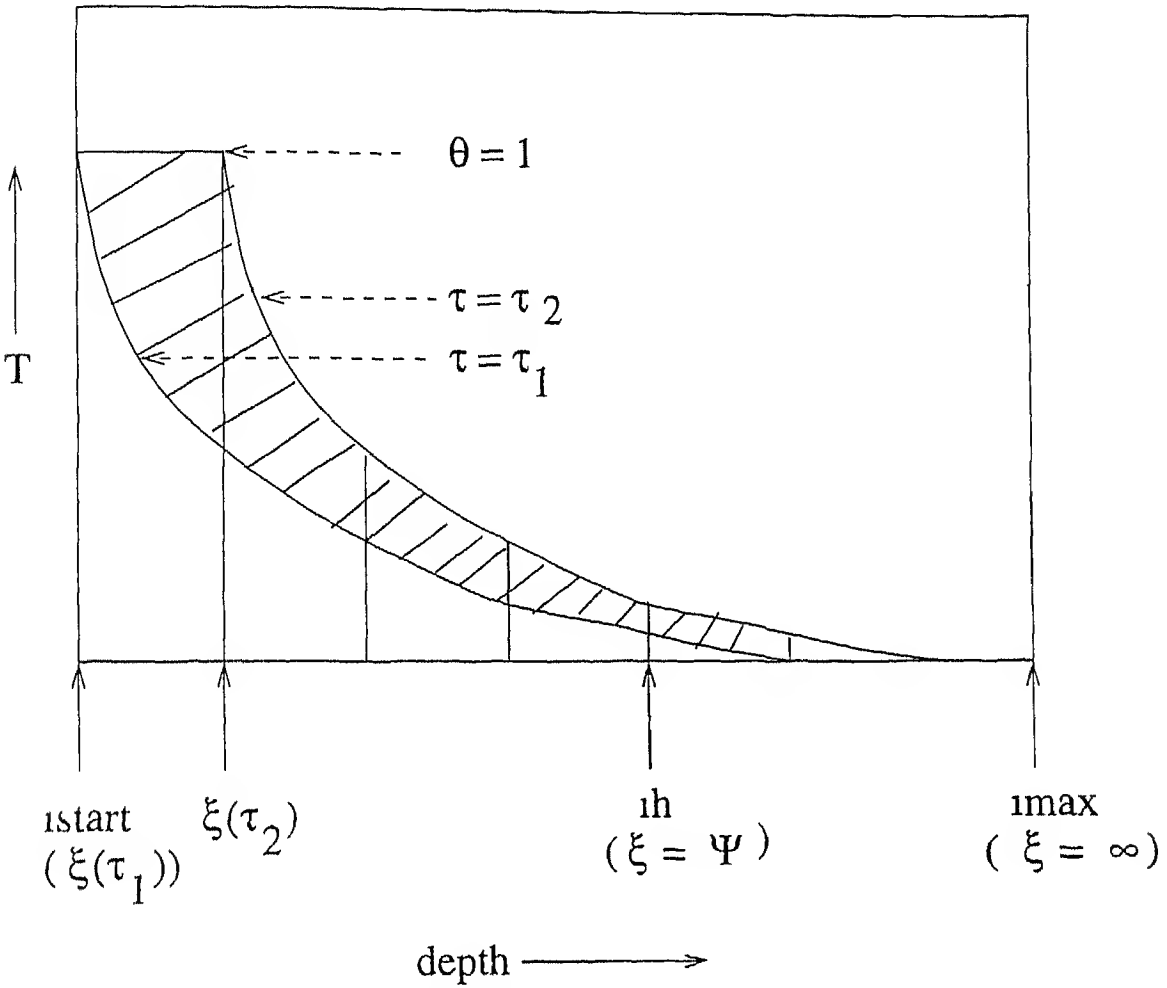


Figure 3 3 Energy balance during laser heating

At $\psi < \zeta < \infty$

$$\frac{a_1}{a_2} \frac{\theta_i^{n+1} - \theta_i^n}{\Delta \tau} = \frac{\theta_{i+1}^{n+1} - 2\theta_i^{n+1} + \theta_{i-1}^{n+1} + \theta_{i+1}^n - 2\theta_i^n + \theta_{i-1}^n}{2\Delta \zeta^2} \tag{3 31}$$

At $\zeta = \infty$

$$\theta_2 = 0 \tag{3 32}$$

The energy balance equation becomes

$$\begin{aligned}
 \frac{q_0 l}{a_1} \Delta \tau = & \rho_1 c_1 (T_m - T_0) \Delta \zeta \left[\left[\sum_{i=i_{start}+2}^{ih-2} \theta_{(i)}^{n+1} \right] + \frac{\theta_{(i_{start}+1)}^{n+1} + \theta_{(ih-1)}^{n+1}}{2} \right] + \\
 & \frac{\rho_1 c_1 + \rho_2 c_2}{2} (T_m - T_0) \Delta \zeta \theta_{(ih)}^{n+1} - \\
 & \rho_1 c_1 (T_m - T_0) \Delta \zeta \left[\left[\sum_{i=i_{start}+1}^{ih-2} \theta_{(i)}^n \right] + \frac{\theta_{(i_{start})}^n + \theta_{(ih-1)}^n}{2} \right] - \\
 & \frac{\rho_1 c_1 + \rho_2 c_2}{2} (T_m - T_0) \Delta \zeta \theta_{(ih)}^n + \\
 & \rho_2 c_2 (T_m - T_0) \Delta \zeta \left[\left[\sum_{i=ih+2}^{imax-1} \theta_{(i)}^{n+1} \right] + \frac{\theta_{(ih+1)}^{n+1} + \theta_{(imax)}^{n+1}}{2} \right] - \\
 & \rho_2 c_2 (T_m - T_0) \Delta \zeta \left[\left[\sum_{i=ih+2}^{imax-1} \theta_{(i)}^n \right] + \frac{\theta_{(ih+1)}^n + \theta_{(imax)}^n}{2} \right] \quad (3.33)
 \end{aligned}$$

The above energy balance equation is used as the basis of an iterative loop. Throughout the finite difference scheme a fixed value of $\Delta \zeta$ is used. While the clad is melting, the time step is taken as the time taken for the phase boundary to move through a distance $\Delta \zeta$. Hence in one time step the phase boundary moves from one grid point to next.

When the surface is moving, an initial value of $\Delta \tau$ is taken and the equations 3.28 to 3.32 are solved. A finite difference approximation using equation 3.33 then yields a revised estimate for the time step $\Delta \tau$, this iteration is repeated until the desired accuracy is achieved before continuing to the next time step.

3.3 Stagnant melting

This physical model assumes a stagnant melt pool of specific thermal conductivity. Effectively, it will become a three layer problem. Here also the temperature distribution during preheating is calculated using equations 3.12

and 3.13 as discussed in the previous section

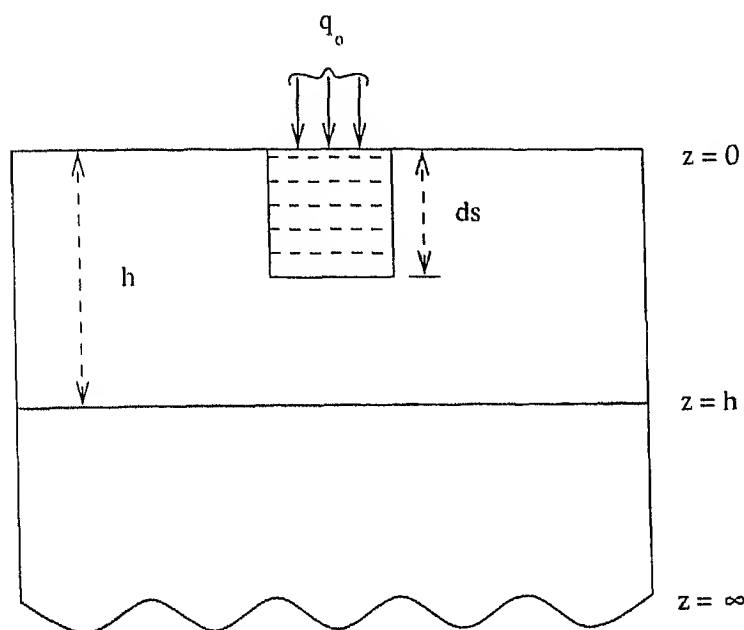


Figure 3.4 Stagnant melting with uniform source

Here the boundary conditions during melting become,

At $z=0$,

$$\lambda_1 \frac{\partial T_1}{\partial z} = q_0 \quad (3.34)$$

At $0 < z < s(t)$,

$$\frac{1}{a_1} \frac{\partial T_1}{\partial t} = \frac{\partial^2 T_1}{\partial z^2} \quad (3.35)$$

At $z = s(t)$,

$$T_1 = T_2 \quad (3.36)$$

$$\lambda_1 \frac{\partial T_1}{\partial z} = \lambda_2 \frac{\partial T_2}{\partial z} \quad (3.37)$$

At $s(t) < z < h$,

$$\frac{1}{a_2} \frac{\partial T_2}{\partial t} = \frac{\partial^2 T_2}{\partial z^2} \quad (3.38)$$

At $z = h$,

$$T_2 = T_3 \quad (3.39)$$

$$\lambda_2 \frac{\partial T_2}{\partial z} = \lambda_3 \frac{\partial T_3}{\partial z} \quad (3.40)$$

At $h < z < \infty$,

$$\frac{1}{a_3} \frac{\partial T_3}{\partial t} = \frac{\partial^2 T_3}{\partial z^2} \quad (3.41)$$

At $z = \infty$,

$$T_3 = T_0 \quad (3.42)$$

Now, the energy balance equation becomes,

$$\begin{aligned} \int_{t_1}^{t_2} q_0 dt &= \int_{t_1}^{t_2} \rho_1 L_m ds(t) + \\ &\int_0^{s(t_2)} \rho_1 c_1 T_1(z, t_2) dz - \\ &\int_0^{s(t_1)} \rho_1 c_1 T_1(z, t_1) dz + \\ &\int_{s(t_2)}^h \rho_2 c_2 T_2(z, t_2) dz - \\ &\int_{s(t_1)}^h \rho_2 c_2 T_2(z, t_1) dz + \\ &\int_h^\infty \rho_3 c_3 T_3(z, t_2) dz - \\ &\int_h^\infty \rho_3 c_3 T_3(z, t_1) dz \end{aligned} \quad (3.43)$$

The above equations [3.34–3.43] in the finite difference form, after normalising using equations 3.14–3.20] are given below

At $\zeta = 0$,

$$\frac{\lambda_1 (T_m - T_0)}{l} \left(\frac{\theta_i^{n+1} - \theta_{i+1}^{n+1}}{\Delta \zeta} \right) = q_0 \quad (3.44)$$

At $0 < \zeta < s(t)$,

$$\frac{\theta_i^{n+1} - \theta_i^n}{\Delta \tau} = \frac{\theta_{i+1}^{n+1} - 2\theta_i^{n+1} + \theta_{i-1}^{n+1} + \theta_{i+1}^n - 2\theta_i^n + \theta_{i-1}^n}{2\Delta \zeta^2} \quad (3.45)$$

At $\zeta = s(t)$,

$$\theta_1 = 1 \quad (3.46)$$

At $s(t) < \zeta < h$,

$$\frac{a_1}{a_2} \frac{\theta_i^{n+1} - \theta_i^n}{\Delta\tau} = \frac{\theta_{i+1}^{n+1} - 2\theta_i^{n+1} + \theta_{i-1}^{n+1} + \theta_{i+1}^n - 2\theta_i^n + \theta_{i-1}^n}{2\Delta\zeta^2} \quad (3.47)$$

At $\zeta = h$,

$$\lambda_2 \left(\frac{\theta_i^{n+1} - \theta_{i-1}^{n+1}}{\Delta\tau} \right) = \lambda_3 \left(\frac{\theta_{i+1}^{n+1} - \theta_i^{n+1}}{\Delta\tau} \right) \quad (3.48)$$

At $h < \zeta < \infty$,

$$\frac{a_1}{a_3} \frac{\theta_i^{n+1} - \theta_i^n}{\Delta\tau} = \frac{\theta_{i+1}^{n+1} - 2\theta_i^{n+1} + \theta_{i-1}^{n+1} + \theta_{i+1}^n - 2\theta_i^n + \theta_{i-1}^n}{2\Delta\zeta^2} \quad (3.49)$$

At $\zeta = \infty$,

$$\theta = 0 \quad (3.50)$$

The above equations [3.44 - 3.50] can be solved by the same iterative method used in the previous section. The finite difference method is validated by comparison with the analytical solution (equations 3.12 and 3.13) for preheating.

Chapter 4

RESULTS AND DISCUSSIONS

4.1 Introduction

Calculations are made for cladding of nickel and stainless steel over C-45 steel. The properties of the materials used are listed below in table 4.1. The density and the specific heat of the liquid metal is not significantly different from that of the solid. Therefore, the liquid clad layer is assumed to have the same density and specific heat as listed above for the corresponding solid [20], except the thermal conductivity. The liquid thermal conductivity is not exactly known.

Table 4.1 Thermal properties of substrate and clad materials

Properties	0.45 %C Steel	Nickel	Stainless steel
Thermal conductivity(J/s/K/mm)	0.0589	0.09	0.0163
Density (g/mm ³)	7.849×10^{-3}	8.906×10^{-3}	7.317×10^{-3}
Specific heat capacity(J/K/g)	0.461	0.444	0.461
Latent heat of fusion(J/mm ³)	2.1	2.000	2.134
Melting point(K)	1673	1673	1723
Boiling point(K)	3273	3173	3273
Thermal diffusivity(mm ² /s)	0.001628	0.002276	0.000483

The melt thermal conductivity for liquid Zn and Sn are about 50% of the thermal conductivity of the corresponding solids [23]. Therefore, thermal conductivities of liquid Ni and stainless steel are assumed to be half that of the corresponding solids. Initial temperature of the clad and substrate are considered as the room temperature (300 K). The clad height is varied from 0.2 mm to 1 mm.

4.2 Preheating

The temperature distribution during preheating is calculated using equations 3.12 and 3.13. The preheating time (till the surface reaches melting point) is calculated iteratively by choosing an initial value of 0.1 s and calculating the clad temperature at the surface. The error in calculated preheat time is kept below 10^{-6} s.

Fig. 4.1 shows the temperature distribution obtained for cladding of nickel over steel at clad height of 1 mm and power densities of 100, 150 and 200 W/mm^2 . The temperature gradient along the depth is very high. The temperature decreases exponentially from the surface to the interior. With increase of power density the temperature gradient increases and the heat penetration depth reduces. The heat penetration is ≈ 3 mm at a power density of 100 W/mm^2 and it drops to ≈ 1.5 mm when the power density is doubled (200 W/mm^2). At the clad-substrate interface a discontinuity in change of slope is observed because of the change in thermal diffusivity at the interface. The temperature gradient in the clad and the substrate are different. Fig. 4.2 shows the temperature distribution for cladding of nickel over steel as well as cladding of stainless steel over steel for 1 mm clad thickness and 100 W/mm^2 power density. The temperature gradient is much higher for stainless steel clad due to its lower thermal diffusivity. Hence, the heat penetration depth

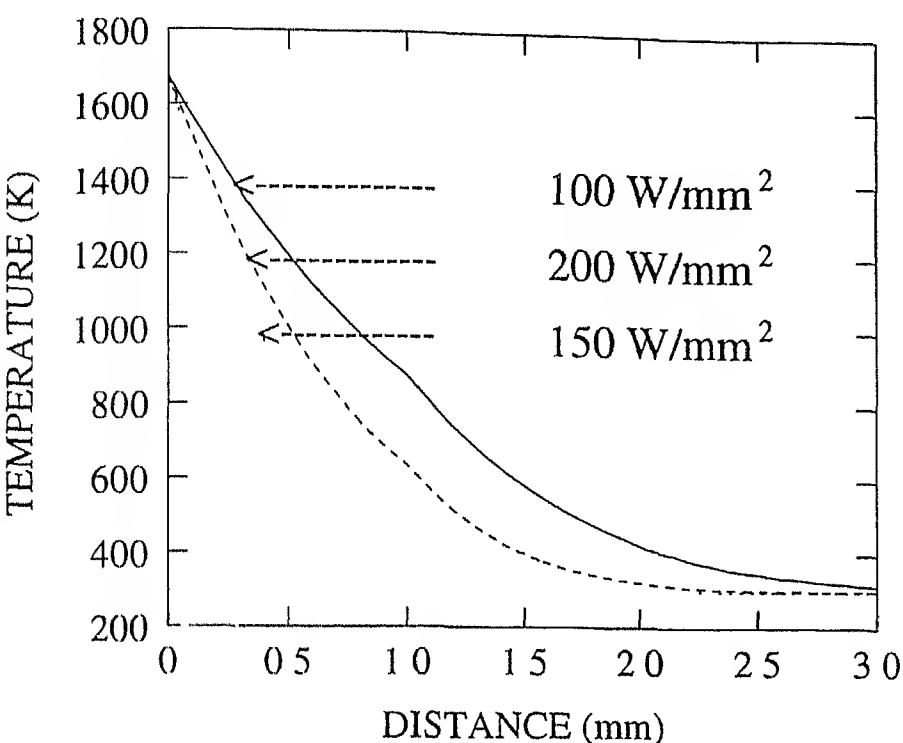


Figure 4.1 Temperature distribution at start of melting of Ni clad over steel at 1 mm clad thickness

is much smaller for stainless steel clad (≈ 0.5 mm) as compared to that for nickel clad (≈ 3 mm)

Fig 4.3 shows the preheat time vs power density for Ni clad at 0.2 mm, 0.5 mm, 1.0 mm thicknesses. The preheat time increases with increase in clad height and with decrease of power density. The increase of Ni clad thickness increases heat dissipation to the interior due to its higher thermal diffusivity than steel substrate and hence the surface reaches the melting point at a later time. Increase of power density increases the heat input rate and reduces heat penetration to the interior, hence the surface reaches the melting point earlier. Fig 4.4 shows the preheat time vs power density for Ni and stainless steel clads with 1 mm thickness and at 100 W/mm^2 power density. The preheating time for nickel is more than that for stainless steel clad for a given clad thickness and power density. This is due to the smaller thermal

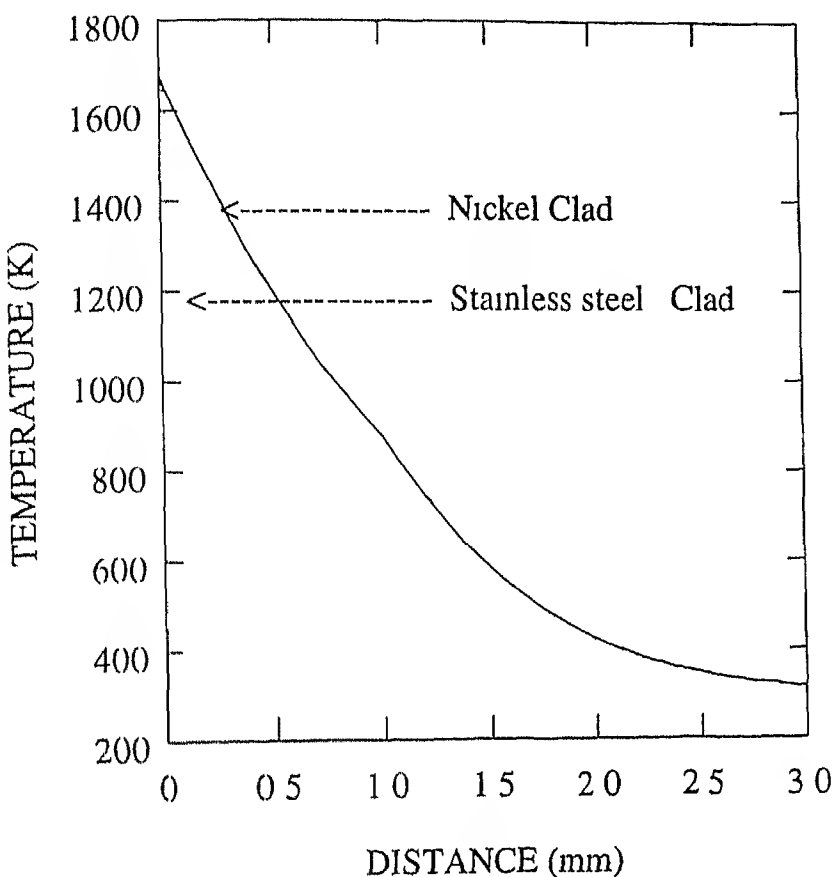


Figure 4.2 Temperature distribution at start of melting 1 mm thick Ni and stainless steel clads at 100 W/mm^2 power density

diffusivity of stainless steel ($0.0005 \text{ mm}^2/\text{s}$) than nickel ($0.0023 \text{ mm}^2/\text{s}$). The smaller thermal diffusivity leads to less heat dissipation to the interior and hence most of the heating occurs at the surface and thus reduces the preheat time. The difference in preheating time reduces as power density increases due to the smaller thermal penetration at a higher power density.

4.3 Turbulent Melting

Here, the melt pool over the solid clad material is assumed to be so turbulent that the melt pool has infinite thermal conductivity. Under these conditions,

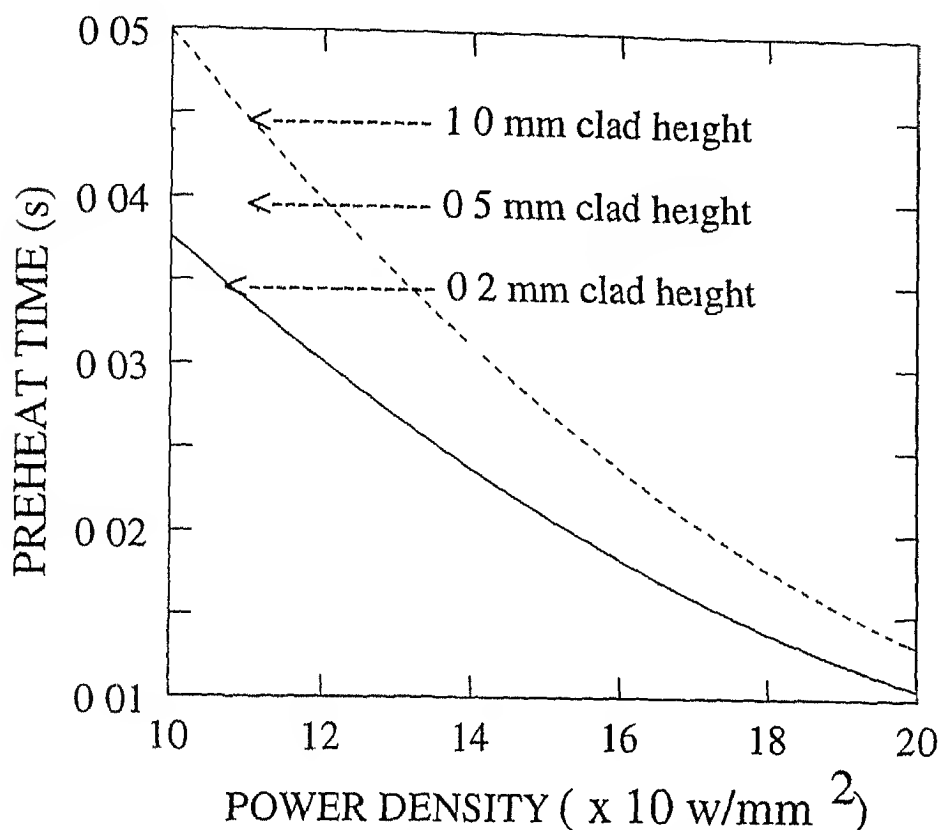


Figure 4.3 Variation of Preheat time with power density of N_1 clad at various clad thicknesses

temperature of the liquid metal is maintained at the melting point. For this case, equations 3.28 to 3.33 are solved by finite difference method as discussed in section 3.2 with Δz as 0.004 mm. The grid size independency is tested with Δz as 0.003 mm and the difference in calculated time for the melt boundary to move to the next grid point is less than 10^{-6} s.

Fig. 4.5 shows the melt boundary migration of 1 mm thick N_1 clad layer over steel at various power densities as a function of time. It shows that the rate of melt boundary migration increases as melting proceeds. This is because the steel substrate has lower thermal diffusivity than the nickel clad and hence less heat will be dissipated to the interior substrate as melting proceeds. Fig. 4.6 shows the melt boundary migration of 1 mm thick stainless steel clad layer

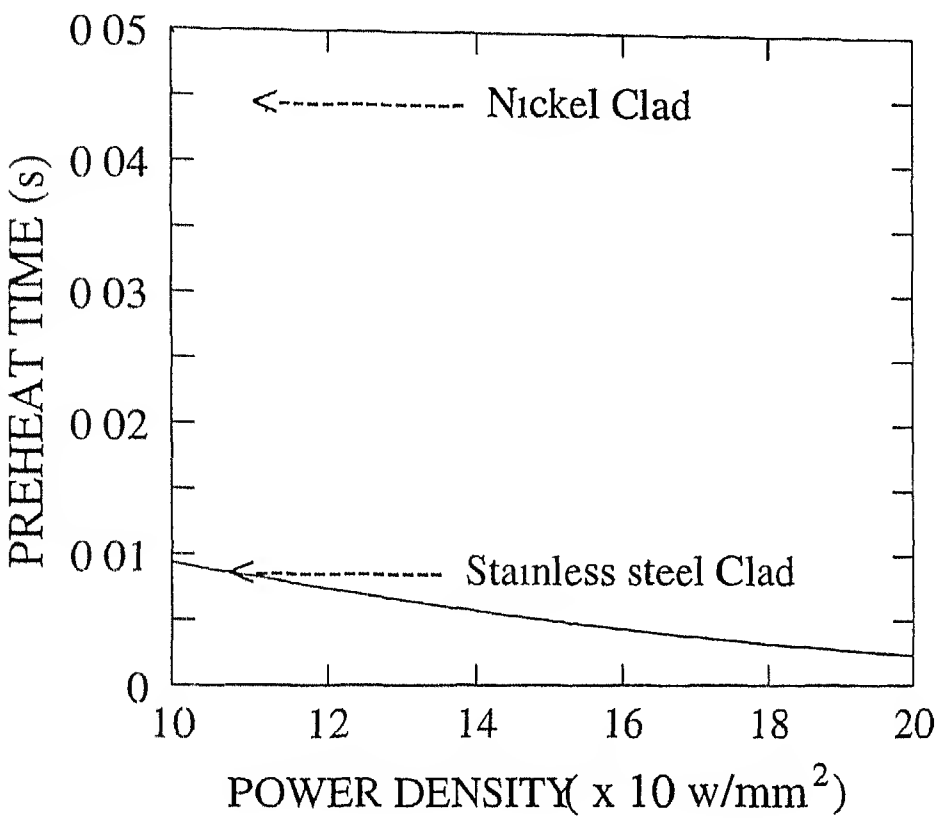


Figure 4.1 Variation of Preheat time with power density for Ni and stainless steel clads over steel at 1 mm clad thickness

over steel at various power densities as a function of time. Contrary to Ni clad, the rate of melt boundary migration for stainless steel clad decreases as melting proceeds. This is due to higher thermal diffusivity of the steel substrate than that of stainless steel. The higher thermal diffusivity increases the heat dissipation into the substrate. Both figures 4.5 and 4.6 show that the rate of melting increases with increase of power density. This is due to the smaller heat penetration into the substrate at higher power density.

Tables 4.2 and 4.3 show the average rate of melt boundary migration, the preheat time, and melting time for Ni and stainless steel clad over steel at various power densities and clad thicknesses. As seen from these tables, the melting time is of the order of fraction of a second. The tables show that the

Table 4.2 Results obtained for cladding of Ni over steel by turbulent model

Power density (W/mm^2)	Clad height (mm)	Preheat time (s)	Melting time (s)	Average melting rate (mm/s)	Heat input J/mm^3
100	1.0	0.050	0.120	14.3	12.0
150	1.0	0.023	0.075	19.2	11.3
200	1.0	0.013	0.052	25.6	10.4
100	0.5	0.044	0.086	11.9	17.2
150	0.5	0.021	0.048	18.5	14.4
200	0.5	0.012	0.032	25.0	12.8
100	0.2	0.038	0.057	10.5	28.5
150	0.2	0.018	0.030	16.7	22.5
200	0.2	0.011	0.019	25.0	19.0

Table 4.3 Results obtained for cladding of stainless steel over steel by turbulent model

Power density (W/mm^2)	height (mm)	time (s)	time (s)	rate (mm/s)	(J/mm^3)
100	1.0	0.009	0.112	9.7	11.2
150	1.0	0.004	0.067	15.9	10.1
200	1.0	0.002	0.050	20.8	10.0
100	0.5	0.009	0.075	7.6	15.0
150	0.5	0.004	0.041	12.3	12.3
200	0.5	0.002	0.029	18.5	11.6
100	0.2	0.011	0.052	4.9	26.0
150	0.2	0.004	0.026	9.1	19.5
200	0.2	0.002	0.017	13.3	17.0

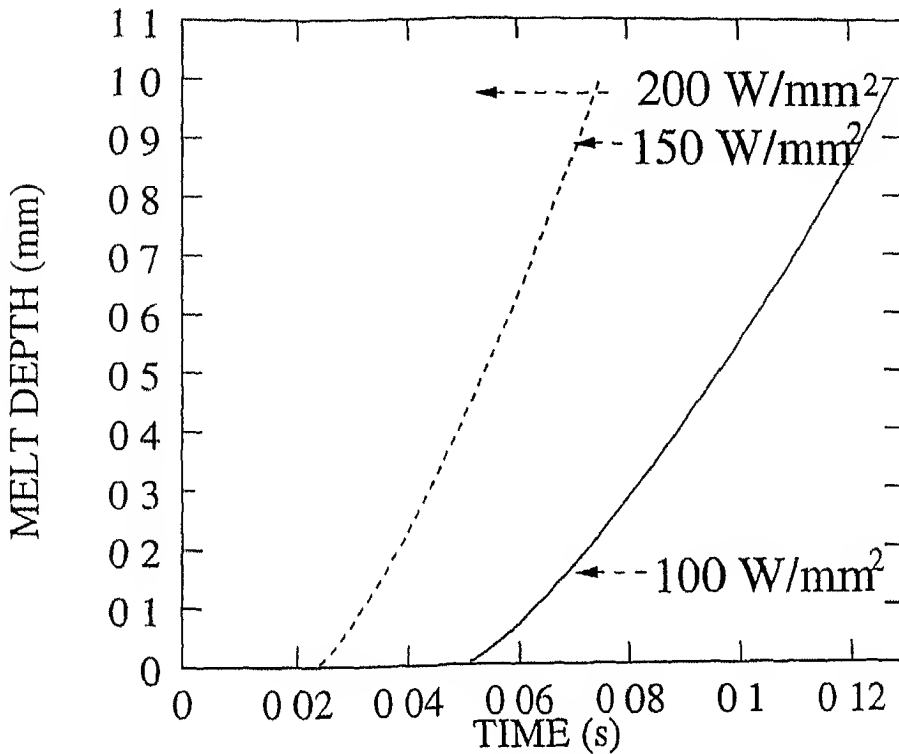


Figure 4.5 Melt boundary migration with time for 1 mm thick Ni clad over steel at various power densities

preheat time for Ni clad is significant. The preheat time for Ni clad over steel is 30-50 % of the total melting time whereas that for stainless steel is only 10-15 %. The total melting time for stainless steel clad over steel is always less than that of nickel over steel for a given clad thickness due to lower thermal diffusivity of stainless steel. As seen from the tables 4.2 and 4.3, for a given power density, stainless steel clads start melting at the same time irrespective of the clad thickness. This is because, the heat penetration depth is less than the clad thicknesses.

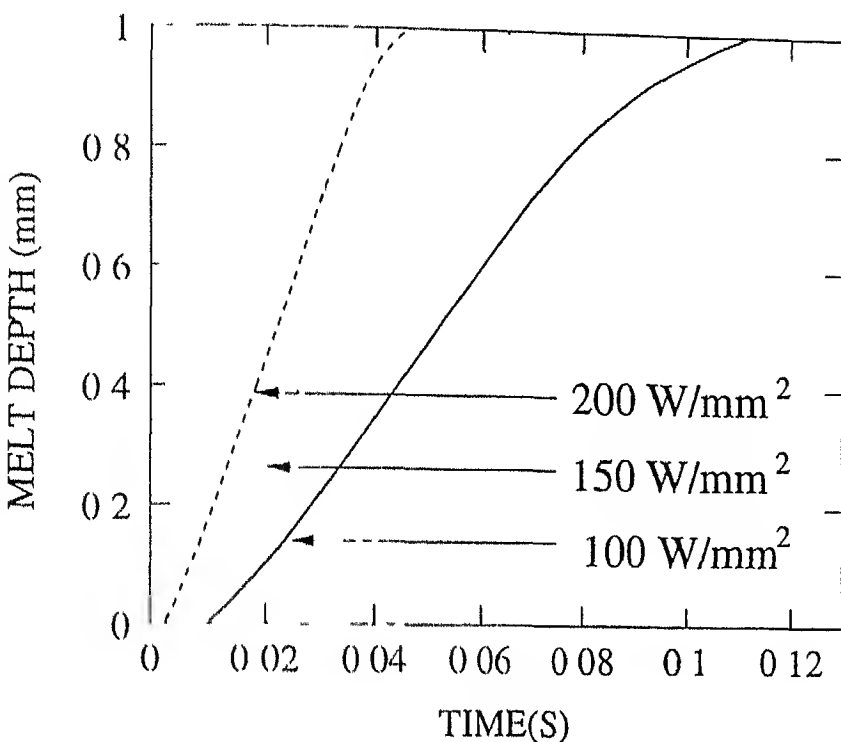


Figure 16 Melt boundary migration with time for 1 mm thick stainless steel clad over steel at various power densities

4.4 Stagnant Melting

Here, the clad melt layer is assumed to be stagnant i.e. no convection in the melt pool, and the heat transfer from the melt to the clad-melt interface is due to only thermal conduction. For this case, finite difference equations 3.44 to 3.50 are solved as discussed in section 3.2 with Δz as 0.004 mm. The grid size independency is tested with Δz as 0.003 mm and the difference in calculated time for the melt boundary to move to the next grid point is less than 10^{-6} s. Calculations at high power densities predict surface temperatures much higher than that the boiling point of the liquid clad layer. Hence, calculations are made for cladding at power densities lower than those used in turbulent melting model.

Fig 4.7 shows the melt boundary migration along the depth as a function

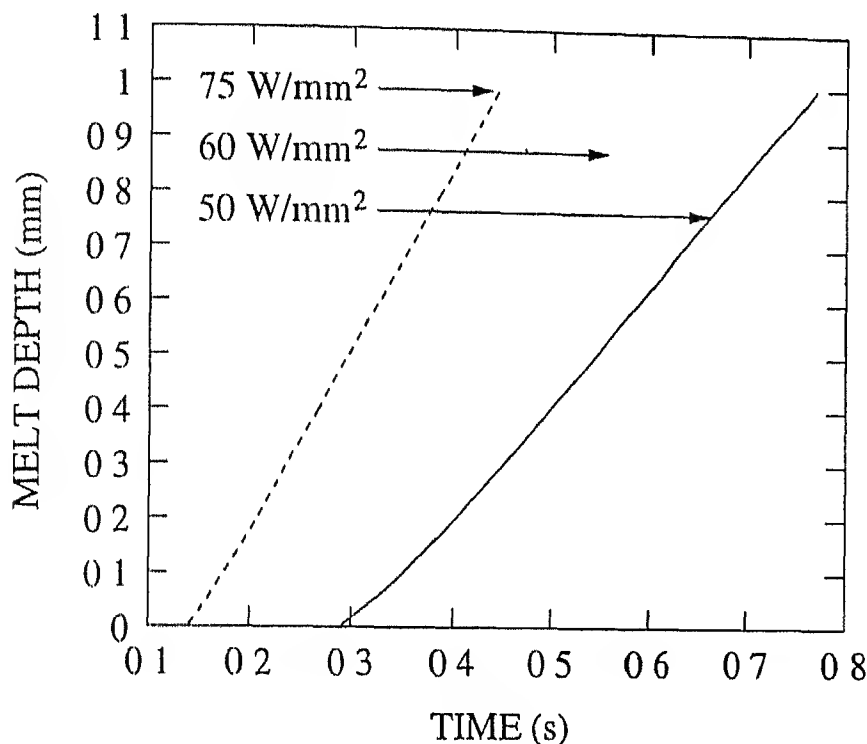


Figure 17 Melt boundary migration with time for 1 mm thick Ni clad over steel at various power densities

of time at power densities of 50, 60 and 75 W/mm^2 for Ni clad of 1 mm thickness over steel. The rate of melt boundary migration decreases as melting proceeds. A small increase in melt boundary migration rate is obtained in the beginning as in the turbulent melting case, but as melting proceeds the thermal barrier due to the liquid melt dominates and hence migration rate decreases. Fig. 18 shows the rate of melt boundary migration of stainless steel clad over steel at power densities of 10, 12, and 20 W/mm^2 . Melting of stainless steel clad starts earlier than nickel and the decrease of melting rate is more for stainless steel clad layer and completion of clad melting occurs later than that of nickel clad. The time for completion of melting decreases continuously as power density increases. The melt boundary migration rate increases with increase of power density and with decrease of clad thickness. Figs. 4.9 and 4.10 show the temperature distribution at the end of cladding. The surface

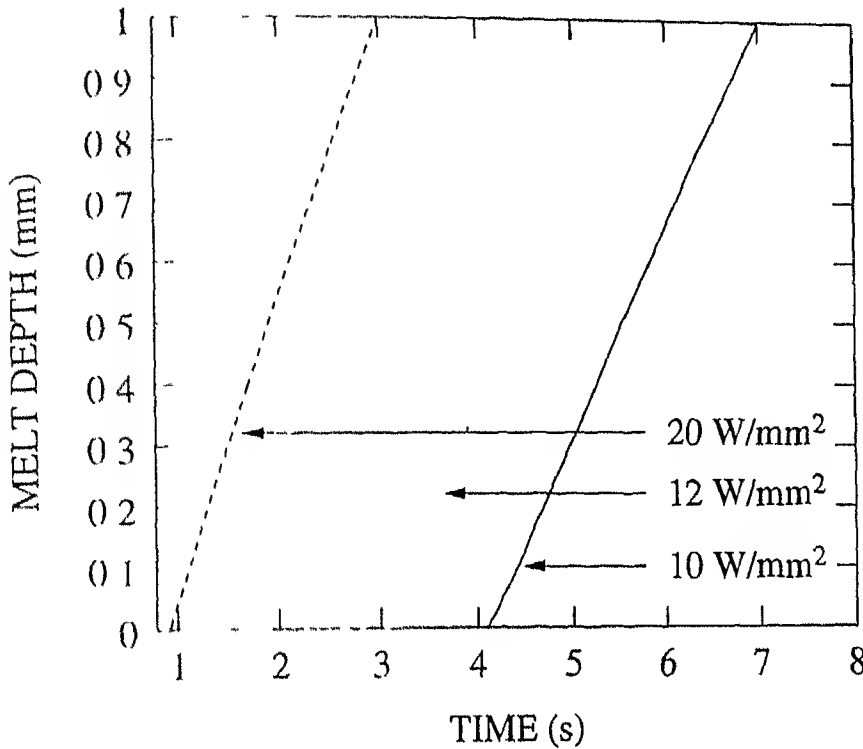


Figure 18 Melt boundary migration with time for 1 mm thick stainless steel clad over steel at various power densities

temperature increases with increase of power density

Tables 4.4 and 4.5 show the average rate of melt boundary migration, the preheat time, melting time and surface temperature for Ni and stainless steel clads over steel at various power densities. The melting rate increases with increase of power density. The heat input required to melt a given clad thickness decreases with increase of power density. This is because of less heat penetration into the substrate at a higher power density. Hence, a power density as high as possible should be used. But, both the tables 4.4 and 4.5 show that the surface temperature increases with increase of temperature. When the surface temperature is above the boiling point of the liquid melt, evaporation occurs at the surface leading to loss of metal and the cladding will not be effective. So the maximum power density that can be used is limited.

Table 4.1 Results obtained for cladding of Ni over steel by stagnant melting model

Power density (W/mm^2)	Clad height (mm)	Preheat time (s)	Melting time (s)	Average melting rate (mm/s)	Heat input (J/mm^3)	Surface temperature (K)
50	1	0.176	0.769	1.67	38.5	2695
60	1	0.126	0.601	2.11	36.1	2883
75	1	0.085	0.449	2.75	33.7	3156
100	1	0.050	0.252	4.95	25.2	3561
75	0.5	0.074	0.115	12.2	43.1	2694

Table 4.5 Results obtained for cladding of stainless steel over steel by stagnant melting model

Power density (W/mm^2)	Clad height (mm)	Preheat time (s)	Melting time (s)	Average melting rate (mm/s)	Heat input (J/mm^3)	Surface temperature (K)
10	1	1.762	7.01	0.191	70.1	2872
12	1	1.080	5.71	0.266	68.5	3095
20	1	0.273	3.00	0.367	60.0	3979

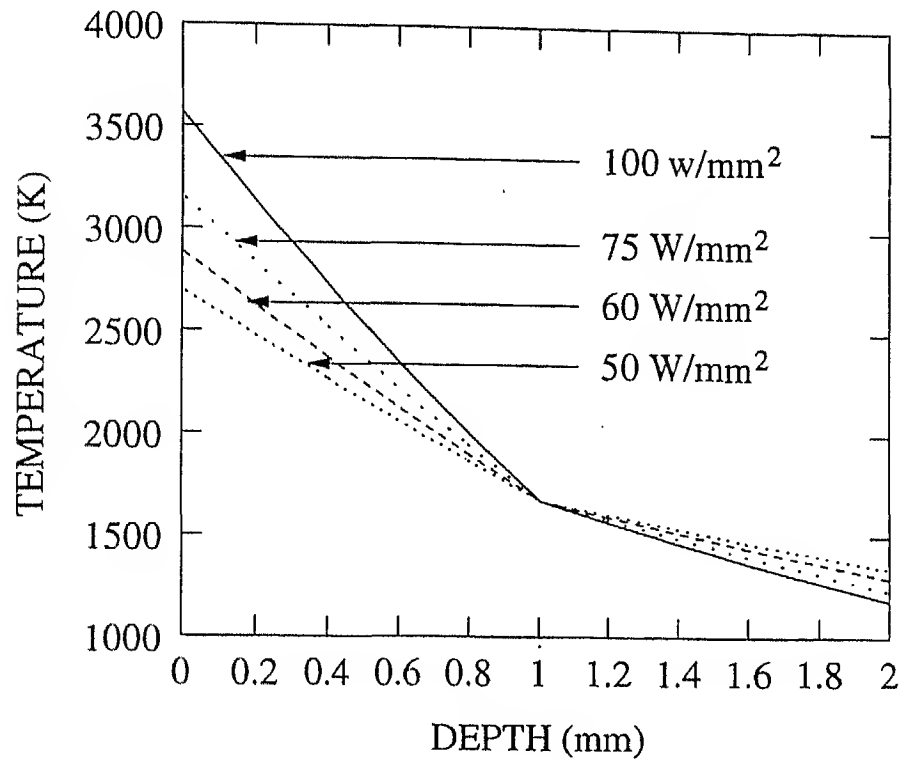


Figure 4.9: Temperature distribution at the end of cladding for 1 mm thick Ni clad over steel at various power densities

by surface evaporation. Hence, from the tables 4.4 and 4.5 the maximum power density that can be used without surface evaporation is 75 W/mm^2 for Ni clad over steel and 12 W/mm^2 for stainless steel over steel, at 1 mm clad thickness. A clad melt layer with lower thermal diffusivity shows higher surface temperature. This model predicts a lower melting rate for a lower thermal diffusivity clad.

4.5 Comparison of the Two Models

The stagnant melting model always predict a higher melting time than the turbulent melting model. For a given power density and clad thickness the turbulent model predicts a lower melting time for a clad with lower thermal

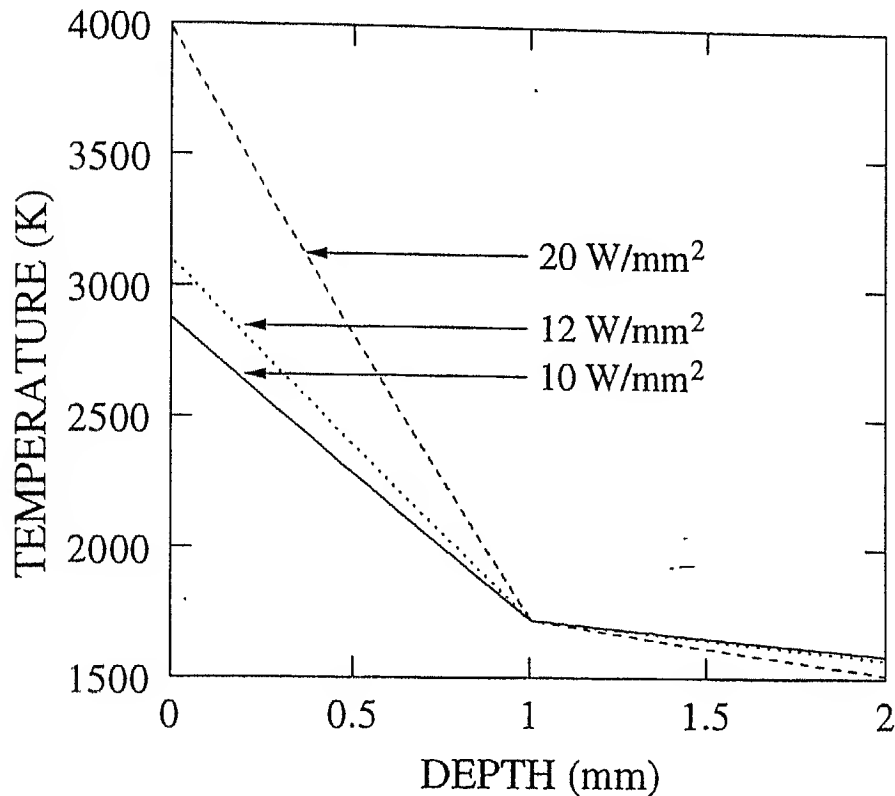


Figure 4.10: Temperature distribution at the end of cladding for 1 mm thick stainless steel clad over steel at various power densities

diffusivity. For both cases, the melting rate increases with increase of power density. The total heat input required also reduces with increase of power density, since the heat penetration into the substrate is less at a higher power density. The turbulent melting model has no limit on the maximum power density that can be used. But, the stagnant melting model predicts the maximum power density above which surface evaporation of the clad melt occurs.

Fig 4.11 shows an example of the melt boundary depth as a function of time for both models for cladding of 1 mm thick Ni clad over steel at 100 W/mm^2 power density. It shows that melting starts at the same time. As melting proceeds the time gap for melting a given depth goes on increasing. Hence, for small melt depth the difference in calculated melt time for the two models is small, but for large depth the difference is significant. This is

CENTRAL LIBRARY
I. I. T., KANPUR

Acc. No. A

124451

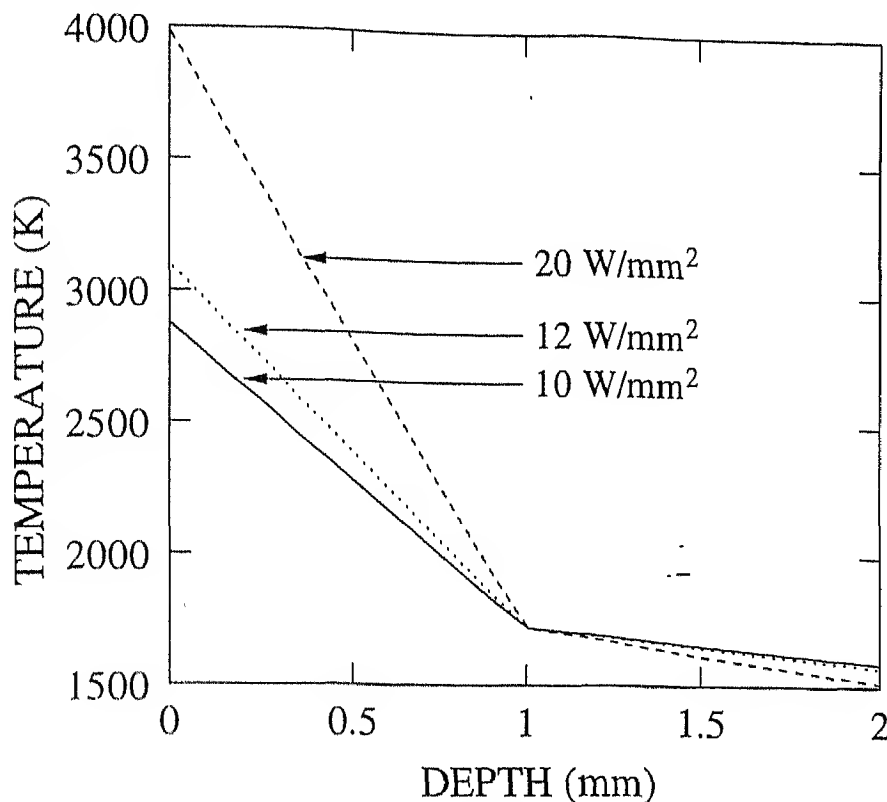


Figure 4.10: Temperature distribution at the end of cladding for 1 mm thick stainless steel clad over steel at various power densities

diffusivity. For both cases, the melting rate increases with increase of power density. The total heat input required also reduces with increase of power density, since the heat penetration into the substrate is less at a higher power density. The turbulent melting model has no limit on the maximum power density that can be used. But, the stagnant melting model predicts the maximum power density above which surface evaporation of the clad melt occurs.

Fig 4.11 shows an example of the melt boundary depth as a function of time for both models for cladding of 1 mm thick Ni clad over steel at 100 W/mm^2 power density. It shows that melting starts at the same time. As melting proceeds the time gap for melting a given depth goes on increasing. Hence, for small melt depth the difference in calculated melt time for the two models is small, but for large depth the difference is significant. This is

CENTRAL LIBRARY
I. I. T., KANPUR

Acc. No. A

124451

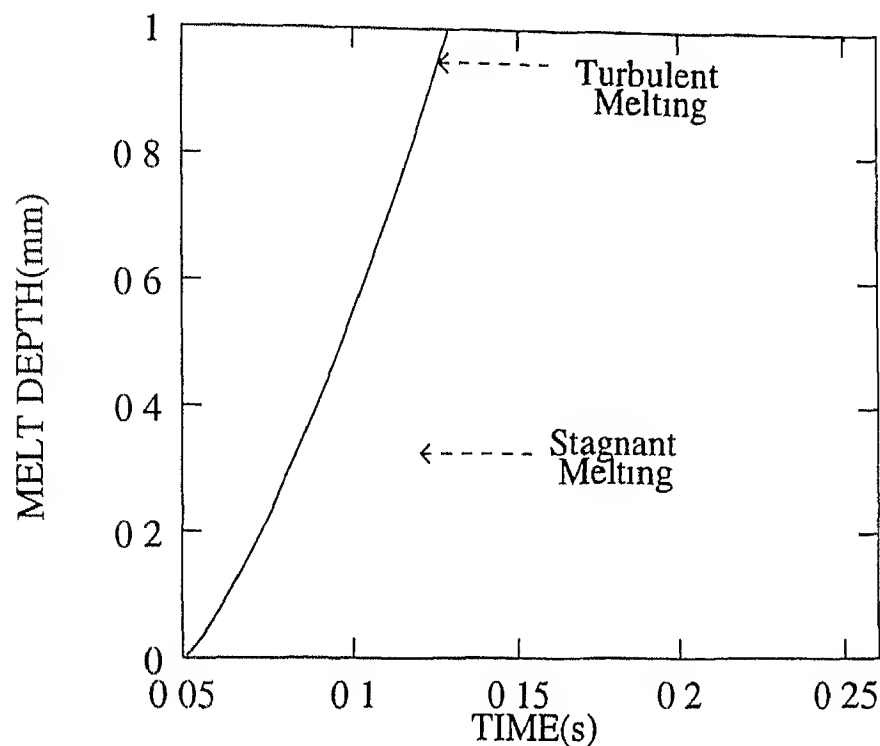


Figure 4.11 Comparison of melting rate of the two models of 1 mm thick Ni clad over steel at 100W/mm^2 power density

because, at small melt depths the heat transfer occurring in the clad melt is not significant

The actual situations would in general be somewhere in-between the extreme conditions considered in the two models. However, it is not easy to model the level of turbulence in the liquid and its effective thermal diffusivity. The turbulence occurring in the melt would in general depend on the power density, the thickness of the melted layer and thermal gradients; hence, it will also be a function of time, as melting proceeds. Turbulence at the start of melting is negligible. As melting proceeds, the melt clad thickness increases and hence the turbulence is expected to increase. As turbulence increases, effective thermal diffusivity of the liquid melt increases. Now, more heat reaches the liquid/solid interface and hence the melting occurs at a faster rate.

The actual melting time in general would be somewhere in-between the melting times predicted by the two models. At small clad heights and small power densities the melting time predicted by stagnant melting model is expected to be closer to the actual melting time. The difference in the melting time predicted by either model is small at small clad thicknesses. Hence, the melting time predicted by either model may be used as a first approximation. At large clad thickness and large power densities the actual melting time is expected to be closer to, but somewhat more than the melting time predicted by turbulent melting model.

Finally, at very high power densities, large amount of energy is absorbed in a very thin layer. At power densities higher than a certain value, direct evaporation may occur with little or no melting. At these power densities, the cladding or surface melting is not possible and even the turbulent melting model breaks down.

In summary, it may be concluded that the turbulent melting model can be used to predict the melting times as a first approximation, during laser cladding at intermediate power densities. The actual melting time is expected to be somewhat larger than the melting time predicted by this model. The stagnant melting model seems to be unrealistic, particularly at high clad thicknesses.

Chapter 5

CONCLUSION

-

Laser cladding process with preplaced powder and with uniform, stationary source is modeled in one dimension. Since melt turbulence is not known, the two extreme cases, with complete turbulence and without turbulence, are modeled. Calculations are made for nickel and stainless steel clads over 0.45 % carbon steel at various power densities and clad thicknesses for parametric study. The following conclusions are derived from the predicted results

1. Both models predict a very small melting time of the order of a fraction of a second to few seconds.
2. The preheat time is significant in comparison to the total melting time for clad materials with higher thermal diffusivity due to higher heat penetration into the interior. The preheat time for Ni clad over steel is 30-50 % of the total melting time, but the preheat time for stainless steel clad is only 10-15 % of the total melting time. Stainless steel has lower thermal diffusivity.
3. Most of the heat absorbed is used for melting the clad.

- 4 The heat penetration depth is in the order of a few millimeters. So, the interior metal properties and microstructure will remain unaffected.
- 5 The total power input required to melt unit volume of the clad material decreases and the melting rate increases with increase of power density.
- 6 The actual melting time would in general be higher than the melting time predicted by turbulent melting model and smaller than the melting time predicted by stagnant melting model. The difference in the predicted melting time for both models is small at small clad thickness. Hence, the melting time predicted by either model may be used at small clad thickness. At large clad thickness and large power densities the actual melting time is expected to be closer to, but somewhat more than the melting time predicted by turbulent melting model.
- 7 It is suggested that the turbulent melting model may be used to estimate the melting times for the clad materials during laser cladding with preplaced powder and with uniform, stationary laser source. The actual melting time is expected to be somewhat more than the predicted melting time.

References

- [1] V. Weerasinghe and W. Steen, "Laser cladding with pneumatic powder delivery system," in *Lasers in Materials Processing*, pp. 166-237, 1983.
- [2] Y. Liu, J. Koch, J. Mazumder, and K. Shibata, "Processing, microstructure, and properties of laser-clad Ni alloy FP-5 on Al alloy AA333," *Metallurgical and Materials transactions B*, vol. 25B, pp. 425-434, June, 1994.
- [3] Y. Liu, J. Mazumdar, and K. Shibata, "Laser cladding of Ni-Al bronze on Al alloy AA333," *Metallurgical and Materials Transactions B*, vol. 25B, pp. 749-759, October, 1994.
- [4] G. Coquerelle, M. Collin, and J. Fachinetti, "Laser cladding and alloying," in *Lasers in Manufacturing*, pp. 197-205, 1983.
- [5] W. Cerni et al., "Laser deposition of carbide reinforced coatings," *Surface and Coatings Technology*, vol. 49, pp. 40-45, 1991.
- [6] J. Com-Nougue and E. Kerrand, " CO_2 laser deposition of a cobalt base alloy on a 12% chromium steel," in *Lasers in Manufacturing*, pp. 191-195, 1985.
- [7] J. Singh and J. Mazumder, "In-situ formation of Ni-Cr-Al-R.E. alloy by surface cladding with mixed powder feed," in *Lasers in Manufacturing*, pp. 169-179, 1985.

- [8] R MacIntyre, "Laser hard-surfacing of turbine blade shroud interlocks," in *Lasers in Materials processing*, pp 230-237, 1983
- [9] G Abbas and D West, "Laser surface cladding of stellite and stellite-SiC composite deposits for enhanced hardness and wear," *Wear*, vol 143, pp 353-363, 1991
- [10] M C Jeng, L Y Yan, and J L Doong, "Wear behaviour of cobalt-based alloys in laser surface cladding," *Surface and Coatings Technology*, vol 48, pp 225-231, 1991
- [11] Weerasinghe, W Steen, and D West, "Laser deposited austenitic stainless steel clad layers," *Surface Engineering*, vol 3, no 2, pp 147-153, 1987
- [12] S Mathews, "Laser fusing of hardfacing alloy powders," in *Lasers in material processing*, pp 138-148, 1983
- [13] L Lugscheider, H Bolender, and H Krappitz, "Laser cladding of paste bound hardfacing alloys," *Surface Engineering*, vol 7, no 4, pp 341-344, 1991
- [14] Y Kogan, "Theory and practice of surface alloying of iron, aluminium, copper, and titanium alloys during laser heating," *Steel in the USSR*, vol 21, pp 370-372, August 1991
- [15] N Rykalin et al, *Laser and Electron Beam Material Processing - Handbook* Mir Publishers, Moscow, 1988
- [16] E N Sobol, *Phase Transformations and Ablation in Laser-Treated Solids* John Wiley and sons, Newyork, 1995
- [17] A Kai and J Mazumder, "One-dimensional finite-medium diffusion model for extended solid solution in laser cladding of Hf on nickel," *Acta Metallurgica*, vol 36, no 3, pp 701-712, 1988

- [18] P. Steen, P. Elnhard, and A. Schussler, "Depth of melt-pool and HAZ in laser surface treatments," *Metallurgical and Materials Transactions A*, vol. 25A, pp. 427-435, Feb' 1994
- [19] S. Kon and Y. Wang, "Three-dimensional convection in laser melted pools," *Metallurgical Transactions A*, vol. 17A, pp. 2265-2270, Dec' 1986
- [20] M. Picasso et al., "A simple but realistic model for laser cladding," *Metallurgical and Materials Transactions B*, vol. 25B, pp. 281-291, Apr' 1994
- [21] M. Jam, S. Iyengar, and R. Jain, *Computational Methods for Partial Differential Equations*. Wiley Eastern Ltd, New Delhi, 1994
- [22] S. Kon and D. Sun, "Heat flow during the laser transformation hardening of cylindrical bodies," *Metallurgical Transactions A*, vol. 14A, pp. 1859-1867, Sep' 1983
- [23] C. Gothandaraman and S. Subramanian, *Heat and Mass transfer Data book*. Wiley - Eastern Limited, 1977
- [24] J. Mazumdar and W. Steen, "Heat transfer model for CW laser material processing," *Journal of Applied Physics*, vol. 51(2), pp. 941-947, Feb' 1980
- [25] M. Ashby and K. Easterling, "The transformation hardening of steel surfaces by laser beams - I Hypo-eutectoid steels," *Acta Metallurgica*, vol. 32, no. 11, pp. 1935-1948, 1984
- [26] T. Zacharia et al., "Heat transfer during Nd YAG pulsed laser welding and its effect on solidification structure of austenitic stainless steels," *Metallurgical Transactions A*, vol. 20A, pp. 957-967, May' 1989
- [27] S. Kon, "Welding, glazing, and heat treating - a dimensional analysis of heat flow," *Metallurgical Transactions A*, vol. 13A, pp. 363-371, Mar' 1982

- [28] S Kou, D Sun, and Y Le, "A fundamental study of laser transformation hardening," *Metallurgical Transactions A*, vol 14A, pp 643-653, Apr' 1983
- [29] S Kou and Y Le, "Three-dimensional heat flow and solidification during the autogenous GTA welding of aluminium plates," *Metallurgical Transactions A*, vol 14A, pp 2245-2253, Nov' 1983
- [30] S Kou, "Simulation of heat flow during the welding of thin plates," *Metallurgical Transactions A*, vol 12A, pp 2025-2030, Dec' 1981
- [31] S Charschan, *Lasers in Industry* Van Nostrand Reinhold Company, New York, 1972
- [32] H Carslaw and J Jaeger, *Conduction of Heat in Solids* Clarendon Press, Oxford, 1959
- [33] J Crank and W Hodgkins, "Moving boundary problems in heat flow and diffusion," in *Proceeding of American Metallurgica*, pp xx-yy, 1975
- [34] B Gebhart, *Heat Transfer* Tata - McGraw - Hill Publishing Co Ltd , Bombay, 1961
- [35] L Rubenstein, *Stefan Problem* American Mathematical Society, 1971
- [36] P Schneider, *Conduction Heat Transfer* Addison - Wesley Publishing Co Inc , 1955
- [37] J Mazumdar and K Mukherjee, "Proceedings of the third symposium on laser material processing, Chicago, Illinois," in *Laser Material Processing III*, Sep 26-28, 1988
- [38] A Prokhorov, V Konov, I Olsu, and I Mihailescu, *Laser Heating of Metals* Adam Hilger, Bristol, 1990

A 124451

Date Slip

This book is to be returned on the
date last stamped **A** 124451

MME-1897 M-JCX-DIM1



A124451